



**NTNU – Trondheim**  
Norwegian University of  
Science and Technology

# Docol 600 DL Steel Plates Subjected to Blast Loading

Numerical Simulations and Experimental  
Validation

**Solveig Heggelund**

Civil and Environmental Engineering (2 year)

Submission date: June 2014

Supervisor: Tore Børvik, KT

Co-supervisor: Vegard Aune, KT

Norwegian University of Science and Technology  
Department of Structural Engineering





## MASTER'S THESIS 2014

SUBJECT AREA: Computational Mechanics	DATE: June 10, 2014	NO OF PAGES: 127 + 31
--	------------------------	--------------------------

TITLE:

**Docol 600 DL Steel Plates Subjected to Blast Loading**

Docol 600 DL Stålplater Utsatt for Eksplosjonslast

BY:

Solveig Brita Heggelund



SUMMARY:

The main objective in this thesis is to investigate the dynamic response of a 0.8 mm Docol 600 DL steel plate subjected to blast loading, by comparing results obtained from experiments at Østøya, Norway, with the particle based approach implemented in the non-linear solver Impetus-Afea.

A pure Lagrangian simulation has also been performed in Abaqus/Explicit. A comparison between the estimated pressure from ConWep, the blast-load function included in Abaqus/Explicit which is based on ConWep and the reflected pressure recorded at Østøya is performed. Abaqus/Explicit seem to underestimate the peak pressure for all stand-off distances, while the impulse is overestimated for the stand-off distances above 250 mm.

A parametric study is performed in Impetus-Afea. From the results obtained, it may be assumed that the parameters describing the load, have greater influence on the deflection than the plate properties. Impetus-Afea has proven to recreate the loading conditions and the dynamic response of the steel plates for the given conditions, with a high level of accuracy.

RESPONSIBLE TEACHER: Professor Tore Børvik

SUPERVISOR(S): Professor Tore Børvik and PhDc Vegard Aune

CARRIED OUT AT: Department of Structural Engineering, NTNU







## MASTEROPPGAVE 2014

FAGOMRÅDE: Beregningsmekanikk	DATO: 10.juni 2014	ANTALL SIDER: 127 + 31
----------------------------------	-----------------------	---------------------------

TITTEL:

**Docol 600 DL Stålplater Utsatt for Eksplosjonslast**

Docol 600 DL Steel Plates Exposed to Blast Loading

UTFØRT AV:

Solveig Brita Heggelund



SAMMENDRAG:

Den nylig introduserte partikkelmetoden implementert i det ikke-lineære element-programmet Impetus-Afea, har tidligere vist seg å være svært numerisk robust og regneeffektivt. Målet med denne oppgaven er å undersøke hvor nøyaktig Impetus-Afea er i forhold til forsøk utført på Østøya. Kvadratiske Docol 600 DL stålplater ble utsatt for eksplosjonslast fra ulike avstander. Ved å sammenligne trykket estimert fra ConWep, lastfunksjonen som er implementert i Abaqus /Explicit som er basert på ConWep, og det registrerte trykket fra forsøket, er det antydnet at Abaqus/Explicit underestimerer maksimalt trykk både i senter og langs randen av platene. Impulsen derimot, ser ut til å være overestimert for avstander over 250 mm.

Et parameterstudie er utført i Impetus-Afea. Resultatene tyder på at lastbeskrivelsen har større innflytelse på platen, enn det platens egenskaper har.

Den dynamisk responsen av platene beregnet i Impetus-Afea er svært nøyaktig, sammenlignet med resultatene fra forsøket

FAGLÆRER: Professor Tore Børvik

VEILEDER(E): Professor Tore Børvik og PhDc Vegard Aune

UTFØRT VED: Institutt for konstruksjonsteknikk, NTNU



## MASTER'S THESIS 2014

for

*Solveig Brita Heggelund*

### **Docol 600 DL Steel Plates Subjected to Blast Loading - Numerical Simulations and Experimental Validation**

#### **1. INTRODUCTION**

Design and validation of blast resistant structures are important for the modern society to protect and secure its citizens. Plated structures are commonly used in applications including protective, offshore, automotive and aerospace structures, just to name a few. In the design of protective structures, steel is often the preferred material. The main reasons for this are that steels have high absolute strength and hardness combined with high ductility, low price compared to most other armor materials and excellent load carrying capability and formability. Thin plates of high-strength steels are therefore frequently being used both in civil and military structures. As a consequence, it is necessary to predict the structural response of high-strength steel plates exposed to blast loading. Today's protective design of blast resistant structures are based on the a priori specification of the pressure history acting on the structure, and does not account for the interaction of shock loading and structural response. However, since the response of these structures is highly nonlinear, this may not be an adequate approach as it may result in unphysical results. In reality, the characteristics of the pressure acting on the structure are a function of the structural response, and may therefore be significantly influenced by the displacement of the structure. In this study, the basic idea is to investigate the structural response of high-strength steel plates exposed to blast loading, and evaluate the available computational methods in terms of robustness and effectiveness.

#### **2. OBJECTIVES**

The research project has three main objectives: (1) investigate experimentally the blast resistance of a 400x400x0.8 mm Docol 600 DL steel plate and (2) employ and evaluate numerical computational methods available for the design of such plates.

#### **3. A SHORT DESCRIPTION OF THE RESEARCH PROJECT**

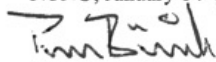
The main topics in the research project will be as follows;

1. A study of current literature: The blast load phenomenon, blast load design, finite element (FE) theory, and suitable material models.
2. Material experiments: Necessary material data sufficient for numerical analyses is to be acquired from previously performed material experiments at SIMLab.
3. Component tests: The dynamic response of the steel plates is studied experimentally, in collaboration with the Norwegian Defence Estates Agency (NDEA), at Østøya by the end of the first quarter of 2014. Free air explosions will be generated using the explosive C4. A Series of blast tests are performed on the plates to determine the dynamic response.
4. Numerical analyses: Non-linear FE numerical simulations of the experiments at Østøya are to be performed. The numerical techniques employed should contain a Lagrangian approach and the newly proposed particle based approach implemented in the numerical code Impetus-Afea Solver.
5. Validation and documentation: The numerical results are to be compared to the experimental findings.

*Supervisors:* Tore Børvik and Vegard Aune (NTNU)

The thesis must be written according to current requirements and submitted to Department of Structural Engineering, NTNU, no later than June 10<sup>th</sup>, 2014.

NTNU, January 14<sup>th</sup>, 2014



Tore Børvik

Main supervisor/Professor



# Abstract

The newly introduced discrete particle approach have previously proven to be numerically robust and computational efficient. The main objective in this thesis is to further investigate the accuracy of the accumulated blast impulse and plate response employing this method, and comparing the results with performed experiments.

Experiments were performed at Østøya, Norway, where quadratic 0.8 mm thick Docol 600 DL steel plates were subjected to free air explosion at stand-off distances 125 mm, 250 mm and 375 mm. The experimental results have been compared with numerical simulations employing the discrete particle method implemented in the non-linear finite element code Impetus-Afea. A pure Lagrangian simulation for a simplified problem have been conducted in Abaqus/Explicit to compare the results with Impetus-Afea.

A comparison between the estimated pressure from ConWep, the blast-load function included in Abaqus/Explicit, which is based on ConWep, and the reflected pressure recorded at Østøya. From the pressure recordings obtained and the calculated impulses, the blast-load function in Abaqus/Explicit seem to underestimate the peak pressure for all stand-off distances, while the accumulated impulse is overestimated when increasing the stand-off distance.

A parametric study is performed in Impetus-Afea to investigate how the plate response is influenced by different parameters. From the results obtained, it may be assumed that the parameters describing the load, have greater influence on the deflection than the plate properties.

Impetus-Afea has proven to recreate the loading conditions and the dynamic response of the steel plates for the given conditions, with a good level of accuracy.



# Acknowledgements

This thesis is written for the Structural Impact Laboratory (SIMLab) and Norwegian University of Science and Technology (NTNU) in collaboration with the Norwegian Defence Estates Agency (NDEA). SIMLab is appointed by the Norwegian Research Council to be a Centre for Research-based Innovation (CRI). SIMLab is engaged in developing methods and tools for the virtual product development of structures exposed to collisions and impact loading. SIMLab is located at the Department of Structural Engineering at NTNU. Industrial and public partners include SINTEF, Hydro Aluminium, leading car manufacturers and NDEA.

Working on this thesis has been highly educational and inspiring. The opportunity to apply non-linear finite element theory and learn about the physics behind shock loading has been a great experience and highly motivating for further work on this subject.

I would like to thank my supervisors professor Tore Børvik and PhDc Vegard Aune at SIMLab for excellent weekly guidance and providing the theoretical background necessary. I would also like to thank Dr. Egil Fagerholt for his contribution with DIC during and after the experiments performed, and Jens Kristian Holmen for his advice regarding the material model and Impetus-Afea.

I would like to thank Knut Ove Hauge, Tore Wisth and Trond Auestad for the work done during the experiments at Østøya, and PhD Knut Gaarder Rakvåg and Svein Olav Christensen for providing pressure values from ConWep.

In addition, I would like to thank Tore André Hustad and Andreas Lyngtveit Lindland for cooperation during the experiment performed and throughout the semester.

Special thanks are given to Dr. Lars Olovsson at Impetus-Afea for his contribution to the numerical model in Impetus-Afea. He has also contributed with great insight to the corpuscular method and troubleshooting in Impetus-Afea.

Trondheim, June 10, 2014

Solveig Brita Heggelund







# Contents

<b>Abstract</b>	<b>i</b>
<b>Contents</b>	<b>ix</b>
<b>Abbreviations</b>	<b>x</b>
<b>1 Introduction</b>	<b>1</b>
<b>2 State-of-the-art</b>	<b>5</b>
<b>3 Theory</b>	<b>9</b>
3.1 Blast physics . . . . .	9
3.1.1 Explosion . . . . .	9
3.1.2 Shock waves . . . . .	11
3.1.3 Failure modes . . . . .	19
3.2 Numerical methods . . . . .	20
3.2.1 Lagrangian and Eulerian FEA . . . . .	20
3.2.2 Explicit time integration . . . . .	22
3.2.3 Kinetic molecular theory . . . . .	26
3.3 Constitutive model . . . . .	32
3.4 Digital Image Correlation . . . . .	35
3.5 ConWep . . . . .	38
<b>4 Material</b>	<b>39</b>
4.1 Docol 600 DL Steel . . . . .	39

4.2	Calibration of Docol 600 DL . . . . .	40
4.2.1	Stresses and strains . . . . .	40
4.2.2	Calibration employing extensometer values . .	42
4.2.3	Calibration employing DIC values . . . . .	44
<b>5</b>	<b>Preliminary study</b>	<b>49</b>
5.1	Mesh sensitivity study . . . . .	49
5.1.1	Procedure . . . . .	49
5.1.2	Results . . . . .	50
5.2	Comparison between Abaqus/Explicit and Impetus-Afea	53
5.2.1	Procedure . . . . .	53
5.2.2	Results . . . . .	54
<b>6</b>	<b>Experiments at Østøya</b>	<b>61</b>
6.1	Experimental set-up . . . . .	61
6.2	Experimental Results . . . . .	68
6.2.1	Blast Loading . . . . .	68
6.2.2	Plate response . . . . .	76
6.2.3	Counter-intuitive reversed snap-buckling . . .	85
<b>7</b>	<b>Numerical simulations</b>	<b>87</b>
7.1	Parameter study . . . . .	87
7.1.1	Results from the different stand-off distances .	89
7.1.2	Boundary conditions . . . . .	91
7.1.3	Number of particles . . . . .	93
7.1.4	Charge weight . . . . .	96
7.1.5	Material model . . . . .	97
7.1.6	Stand-off variations . . . . .	99
7.1.7	Plate thickness . . . . .	101
7.1.8	Counter-intuitive buckling . . . . .	103
<b>8</b>	<b>Discussion</b>	<b>105</b>
8.1	Experiment compared to numerical simulations . . .	105
8.1.1	Abaqus/Explicit vs Impetus-Afea . . . . .	113
8.1.2	Sources of error in the numerical model . . . .	114

8.1.3	Results compared to other experiments and numerical simulations . . . . .	115
<b>9</b>	<b>Concluding Remarks</b>	<b>117</b>
<b>10</b>	<b>Further work</b>	<b>119</b>
	<b>References</b>	<b>120</b>
<b>A</b>	<b>Kingery-Bulmash Chart (Ch. 3.5)</b>	<b>A.1</b>
<b>B</b>	<b>Experimental Results (Ch. 6)</b>	<b>B.1</b>
B.1	Matlab Script . . . . .	B.2
B.2	Pressure Curves from Calibration Tests . . . . .	B.7
B.3	Calculated Impulses for Calibration Tests . . . . .	B.12
<b>C</b>	<b>Preliminary Study (Ch. 5)</b>	<b>C.1</b>
C.1	Keyword Example Abaqus/Explicit . . . . .	C.2
<b>D</b>	<b>Keyword Example Impetus-Afea (Ch. 7)</b>	<b>D.1</b>
D.1	Keyword Example for Pre-Tensioning . . . . .	D.2
D.2	Keyword Example for Blast Simulations . . . . .	D.8

# Abbreviations

$U$	=	Blast front velocity
$P_{so}$	=	Peak static (side-on) overpressure
$P_0$	=	Ambient air pressure in an undisturbed medium
$P$	=	Pressure
$\rho_0$	=	Density of air ambient pressure ahead of the blast wave
$\rho_s$	=	Density behind the wave front
$a_0$	=	The speed of sound in air at ambient pressure
$t_a$	=	Time of arrival
$T^+$	=	Duration of positive phase
$P_{so}^-$	=	Peak static under pressure in negative phase
$T_-$	=	Duration of negative phase
$b$	=	Decay coefficient (Friedlander equation)
$I_s^+$	=	Positive impulse
$I_s^-$	=	Negative impulse
$q_s$	=	Dynamic pressure
$u_s$	=	Particle velocity behind the wave front
$C_0$	=	Initial configuration Lagrange formulation
$C_n$	=	Deformed configuration Lagrange formulation
$t_n$	=	Time step at step n
$D_n$	=	Displacement at time step n
$\dot{d}^n$	=	Velocity at n
$\ddot{d}^n$	=	Acceleration at n
$v^n$	=	Velocity at n
$a^n$	=	Acceleration at n
<b>C</b>	=	Damping
<b>K</b>	=	Stiffness
<b>K<sup>eff</sup></b>	=	Effective stiffness
<b>M</b>	=	Mass

$f^n$	=	Force at n
$f^{ext}$	=	External force
$f^{int}$	=	Ineternal force
$s_f$	=	Safety factor critical time step
$\omega$	=	frequence of structure
$\xi$	=	Parent element coordinates
$\Delta t$	=	Time step
$\Delta t_{cr}$	=	Critical time step
$\dot{u}_t$	=	Velocity at time t
$u_t$	=	Acceleration at time t
$\Delta \varepsilon$	=	Element strain increments
$\varepsilon$	=	Strain rate
$\sigma$	=	Stress
$\sigma_t$	=	Stress at time t
$\mathbf{I}$	=	Internal nodal forces
$f(v)$	=	Probability density function
$M$	=	Molar mass
$R$	=	Universal gas constant
$T$	=	Temperature
$v$	=	Velocity
$v_{rms}$	=	Mean root square velocity
$m$	=	Total mass of the molecules
$W_k$	=	Total translational kinetic energy of the particles
$w_k$	=	Specific translational kinetic energy
$f$	=	Frequency of collision
$j$	=	Transferres impulse
$V$	=	Volume of given box
$p$	=	Average pressure
$A$	=	Area of given box



$e$	=	Total specific energy
$I$	=	Mean-free-path of a particle
$f_c$	=	Frequency of collision
$r_p$	=	molecular radius
$\sigma_{eq} = \phi(\boldsymbol{\sigma})$	=	Equivalent stress
$\sigma_Y = \sigma_0 + R$	=	Flow stress
$\sigma_0$	=	Initial yield stress
$d\boldsymbol{\varepsilon}$	=	Strain increment
$d\boldsymbol{\varepsilon}^e$	=	Elastic strain increment
$d\boldsymbol{\varepsilon}^p$	=	Plastic strain increment
$d\boldsymbol{\varepsilon}^t$	=	Temperature strain increment
$E$	=	Elasticity modulus
$\nu$	=	Poisson's ratio
$\mathbf{I}$	=	Second order unit tensor
$\boldsymbol{\sigma}^{\Delta J}$	=	Jaumann rate of Cauchy stress tensor $\boldsymbol{\sigma}$
$\dot{T}$	=	Rate of temperature
$\alpha$	=	Linear thermal expansion coefficient
$\dot{p}$	=	Equivalent plastic strain rate
$\boldsymbol{\sigma}'$	=	Deviatoric stress tensor
$\sigma_0$	=	Yield stress
$\sigma_{eq}$	=	Equivalent stress
$R$	=	Isotropic hardening
$p$	=	Plastic strain
$A, B, C, n, m$	=	Material constants in Johnson-Cook
$T^*$	=	Homologous temperature
$(T_0, T_m)$	=	Room and melting temperature of the material
$\dot{p}^* = \frac{\dot{p}}{\dot{p}_0}$	=	Dimensionless strain rate

$\dot{p}_0$	=	is a user-defined strain rate
$Q_i, C_i$	=	Material parameters in Voce
$\dot{\varepsilon}$	=	Plastic strain rate
$\dot{\varepsilon}_0$	=	Reference strain rate
$q$	=	Internal variables in the constitutive model
$F$	=	Correlation function F
$i$	=	Specific pixel
$I_r$	=	Reference image
$I_c$	=	Current image
$\Omega$	=	Pixels within the subset at reference configuration
$I_r$	=	Reference image
$\varepsilon_e$	=	Engineering strain
$L$	=	Length of test specimen
$L_0$	=	Initial length of the test specimen
$\Delta L$	=	Elongation of test specimen
$F$	=	Force applied in the extensometer
$A_0$	=	Initial crosssection area
$\sigma_e$	=	Engineering stress
$\varepsilon_e^e$	=	Engineering strain
$\varepsilon_{me}$	=	Measured engineering strain
$\Delta \varepsilon_e$	=	Difference in engineering strain
$E_{corr}$	=	Correct elasticity modulus
$E_{meas}$	=	Measured elasticity modulus
$\varepsilon_l$	=	True strain
$\sigma_t$	=	True stress
$C$	=	Strain rate sensitivity factor
$\varepsilon_l^p$	=	Logarithmic true strain
$Z$	=	Scaled Hopkinson-Cranz distance
$R$	=	Range from the detonation
$W$	=	Charge weight
$D$	=	Rigidity of a plate
$t$	=	Plate thickness
$\theta$	=	Angle of incidence

# Chapter 1

## Introduction

In recent years, protection of structures exposed to blast loading from terrorist attacks have become highly relevant in addition to accidental explosions. To prevent loss of life due to direct blast-effects or structural collapse, design and validation of blast resistant structures are essential. Due to the threat of such extreme loading conditions, efforts are made to further develop methods of structural analysis to resist the blast load. Traditionally, concrete has been the material in use when protecting structures against blast. The main disadvantage using concrete, is the massive weight and inconvenience of the inflexible structure, thus for non-stationary objects a lightweight material is more suitable. The use of plated metal structures have been more widely investigated for stationary structures use as well.

Previous work is primarily performed by the military which carry out full scale explosive tests. The issue with these experiments are that the test specimen is destroyed together with test equipment, and the results may be difficult to interpret [1]. To overcome the problems with full-scale experiments, numerical simulations have proven to be a useful tool to investigate the effect of different blast scenarios.

Until recently, continuum-based Eulerian approaches are regarded

as the most accurate tool when describing the load and structural response in blast load problems.

In the master thesis by Hernandez and Andersen [2], several different numerical techniques have been applied including ALE and the discrete particle approach implemented in the numerical solver Impetus-Afea. The discrete particle approach proved to be the most accurate, in addition to being the easiest to define numerically and having the lowest computational costs.

The motivation behind this thesis is to further investigate the advantages of representing the load and accuracy of the plate response when applying the discrete particle based approach. Numerical simulations of lightweight steel plates subjected to blast loading will be validated against free air explosions performed at Østøya, Norway. The numerical simulations will mainly be carried out in Impetus-Afea.

A short review of each chapter is given below.

**Chapter 2** State-of-the-art. A limited state-of-the-art to display the previous work performed regarding blast theory and the particle based method.

**Chapter 3** Theory. A study of relevant theory to the problem at hand including blast physics, Lagrangian Finite Element Analysis (FEA) and Eulerian FEA, material constitutive relations, Digital Image Correlation (DIC), the discrete particle method and the blast load standard ConWep.

**Chapter 4** Materials. A calibration of a previous material test performed and comparison between material parameters obtained from calibration with extensometer values and calibration based DIC measurements.

## CHAPTER 1. INTRODUCTION

---

**Chapter 5** Preliminary study. A preliminary study is performed to investigate appropriate mesh size. The accuracy between Abaqus/-Explicit and Impetus-Afea is investigated for a simple problem.

**Chapter 6** Experimental work. The set-up and results from the experiment on the steel plates at Østøya is performed.

**Chapter 7** Numerical simulations. The results from the numerical simulations in Impetus-Afea are presented.

**Chapter 8** Discussion. A discussion and comparison between the results obtained from the numerical simulations and the experimental results.



# Chapter 2

## State-of-the-art

Useful to those concerned in research involving the response of the structures subjected to explosive loading, a subject that has become increasingly important with heightened public awareness, is the potential explosive threats to civilian safety. The last four to five decades, the topic has been more closely investigated and it is widely reported. Until the mid of the 1980s, the work reported in the literature was almost exclusively concerning plates and beams [3].

In 1988 Nurick and Martin [4] presented a review of deformation of thin plates subjected to impulsive loading. An empirical relation between the deflection-thickness ratio, function of the impulse, plate geometry, plate dimensions and material properties was presented. During the 1990s their investigations were extended to include the effect of boundary conditions, plate stiffeners, loading conditions and to predict both the deformation and failure. Using these theoretical procedures and empirical relations, the results of analytical studies on the response of plated structures subjected to explosive loading was presented by many researches. In most cases the plastic hinged model, proposed by Jones [5] and Menke [6], was applied to predict

the deflections of the plate.

Besides the analytical analysis performed by the above mentioned researchers, some focused on describing the plate response using the finite element method for structures subjected to impact loading. These have up until the last decade been defined by a purely Lagrangian formulation, typically used for structures.

To calculate the response, the simplified analytical models have been combined with calculations of the blast load propagation and diffraction around structures using an Eulerian solver. Eulerian solvers do not follow the motion of the material particles. The discretizations remain fixed and the material particles flow through it. Hence, this approach is often favourable when simulating fluids and gases. Numerical simulations of coupled problems in fluid dynamics and non-linear solid mechanics often requires coping with great distortions. In attempt to combine the advantages of the above classical kinematical description, a technique has been developed known as the Arbitrary Lagrangian- Eulerian (ALE) description, see for instance [7]. If fluid-structure-interaction (FSI) effects are taken into account, the ALE description considers the deformation of the structure and the corresponding nodes in the fluid mesh employing a contact algorithm [8]. This approach have been implemented in several commercial finite element software like Abaqus/Explicit [9] , Ls-Dyna [10], Autodyn [11] and Europlexus [12].

In Børvik et al. [13], the dynamic response of a structure was compared by employing three different numerical approaches; pure Lagrangian, uncoupled and coupled Eulerian- Lagrangian. The structural response was found to be less for the coupled and the uncoupled Eulerian-Lagrangian, than for the pure Lagrangian with loading conditions based on ConWep. It was observed that the flexibility of the structure reduced the loading. Care must be taken when applying pressure loads from rigid structures onto more flexible ones, as



the structural deformation may be overestimated and vice versa. It was also demonstrated that the accuracy of the time-pressure history from ConWep [14] satisfying, as the pure Lagrangian analysis yielded better results than the fully coupled Eulerian-Lagrangian analysis. However, the test results revealed that the actual blast load was higher than the ones assumed in the simulations. The conservative ConWep data was closer to the applied loading conditions, and thus gave better results. This demonstrate the importance of precise load description. In [15] the efficiency and accuracy of fluid-structure-interaction (FSI) using ALE, were compared to the results of the Lagrangian model and experimental result performed by Boyd [16]. The efficiency and accuracy of FSI and Lagrangian models were proven to be highly accurate when the initial internal energy of air was increased significantly. Extensive work including experiments and validation by numerical simulations using ALE formulation have been performed in recent years. Comparison between numerical models and with experimental observations can be found in [17],[18],[19],[20] and [21], among others. Spranghers have also contributed to the amount of experimental data available and have recently presented full-field measurements for close-range blast in [22], [23] and [24].

In 2007 Olovsson [25], introduced the corpuscular method for airbag deployment simulations, which are based on kinetic molecular theory. This technique have been further developed to a finite element solver for non-linear problems, Impetus-Afea. Impetus-Afea have proven to display accurate results without being as computational expensive as traditional continuum-based Eulerian-Lagrangian approaches. This approach was further investigated in [26] where the ALE approach is compared to the discrete particle method for a reference set-up of a circular steel plate exposed to blast loading from 15 kg TNT at stand-off distance 1000 mm. It was found that the computational time could be significantly reduced, the method was numerically robust and the approach easily copes with complex geometries. In [27] the discrete particle method was compared to the ALE approach imparted in Ls-Dyna on determining the structural response of steel plates subjected

to combined blast and sand impact loading from a buried charge. It was demonstrated that the particle based method was able to predict the physical loading mechanisms of the problem. Good quantitative compliance between Impetus-Afea, Ls-Dyna and the experimental work was obtained.

The discrete particle approach has not been reviewed extensively, but the studies performed display accurate results and computational efficiency. The approach has proven to be a genuine alternative to the traditional FSI algorithms.

# Chapter 3

## Theory

This chapter presents the physics behind blast loading and relevant theory for the problem-at-hand.

Section 3.1 will present basic theory about blast and pressure, Section 3.2 present theory behind the numerical methods applied, Section 3.3 display the Constitutive equations for the material model applied, Section 3.4 introduce the technique behind Digital Image Correlation and Section 3.5 present the load standard ConWep.

### 3.1 Blast physics

#### 3.1.1 Explosion

High-order explosives (HE) are more powerful than lower order explosives (LE). HE detonates and produce a supersonic over-pressurization shock wave. Examples of HE include Trinitrotoluene, C-4, Nitroglycerin and ammonium nitrate fuel oil (ANFO). LE deflagrate to create a subsonic explosion. Deflagration is different from detonations, as deflagration describes a subsonic combustion propagating through heat

transfer at modest overpressure [28]. This process is generally faster than a combustion but slower than a detonation and it lacks the high explosive over-pressurization wave. However, it is possible for LE to deflagrate very quickly, producing an effect similar to a detonation. Sources of LE are pipe bombs, gunpowder and most petroleum-based incendiary bombs such as Molotov Cocktails or aircraft improvised as guided missiles. HE and LE induce different injury patterns. Only HE produce true blast waves. [29] [30]

The more general definition of an explosion is a rapid increase of volume and release of mechanical, chemical or nuclear energy in a sudden and often violent manner with the generation of high temperature and usually with the release of gases. Supersonic explosions created by high explosives are known as detonations and propagate as supersonic shock waves. Fragmentation is the accumulation and projection of particles as the result of a high explosive detonation. Fragmentation could be a part of a structure such as a magazine. High velocity, low angle fragments can travel hundreds of meters with enough energy to initiate other surrounding high explosives items, injure or kill personal and damage structures. [30]

The the different kinds of detonations are categorized as

- Ground burst explosions
- Above-ground explosions
- Below-ground explosions
- Underwater explosions

The experimental work performed in this thesis at Østøya are above-ground explosions and this is what this thesis will mainly focus on.

Even though analysis of loading and response of structures subjected to explosions have been studied for over a century, the lack of uniformity should not be overlooked. Charges of nominally the same weight and geometry do not necessarily yield similar pressures, durations or impulsive characteristics. There are peaks and troughs in the pressure distribution pattern, that make it difficult to treat the loading analysis as an exact science. Experimental scatter is frequently observed in laboratory or field tests. [30]

### 3.1.2 Shock waves

The term blast wave includes both sonic compression waves, shock waves and rarefaction waves. The type of blast wave depends on how and when the energy is released in the explosion and the distance from the explosion area. As illustrated in Figure 3.1 there are three main types of blast

- i) a shock wave followed by a rarefaction wave.
- ii) a shock wave followed by a sonic compression wave and then a rarefaction wave.
- iii) a sonic compression wave and a rarefaction wave.

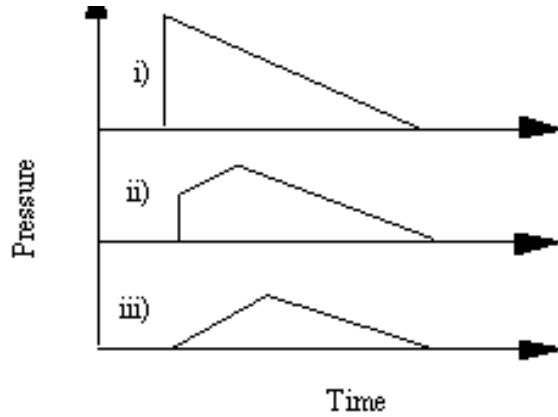
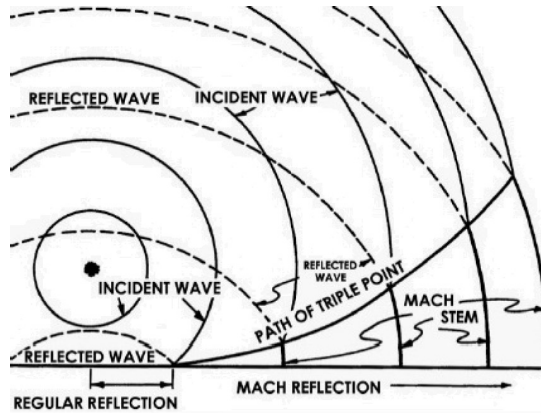


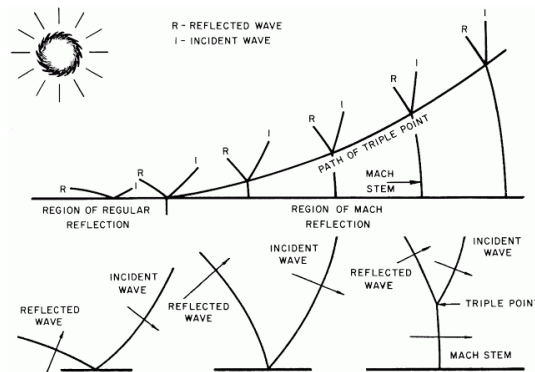
**Figure 3.1:** Main types of blast waves [31].

For strong explosions the first category is typical. Weak explosions is initially the third category, but the wave can steepen (colloquially, "shock up") to category one when it propagates away from the explosion [30]. The resulting shock front moves supersonically, faster than the speed of sound in the air ahead of it. The air molecules behind the shock front moves at lower velocities, namely particle velocities. The pressure from the shock wave consists of both hydrostatic and dynamic pressure [32].

When an explosive source is located a distance above ground, the reflection process is similar to what is shown in Figure 3.2. When the incident wave first impact the flat surface it is reflected, but the reflected shock wave propagate with a higher velocity than the incident shock front. The point where the reflected shock wave overtake the incident shock front, is known as the triple point. The waves merge to a single outward travelling front known as the Mach stem [33].



(a) Reflections of strong shock waves



(b) Mach stem reflection

**Figure 3.2:** Reflections for shock waves for explosions above ground [33].

For blast waves and shock waves the terms hydrostatic pressure and reflected pressure are used. The hydrostatic pressure is also known as the side-on pressure, and it is the pressure that a surface parallel to the shock wave direction would experience as seen in Figure 3.3 [32]. The side-on pressure does not include the dynamic pressure, it

is more like a static overpressure.

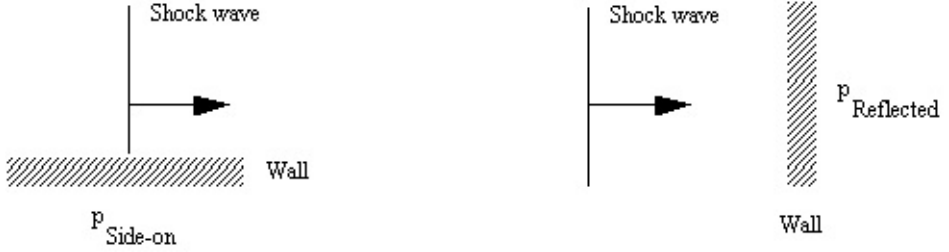


**Figure 3.3:** Side-on and head-on pressure [31].

Of particular importance are the blast wave parameters. The equations for blast front velocity  $U$ , air density behind the wave front  $\rho_s$  and the maximum dynamic pressure  $q_s$  are given below. These are described for normal shocks in ideal gases.

$$U = \sqrt{\left(\frac{6P_{so} + 7P_0}{7P_0}\right)}a_0 \quad (3.1)$$

$$\rho_s = \frac{6P_{so} + 7P_0}{P_{so} + 7P_0}\rho_0 \quad (3.2)$$

$$q_s = \frac{5P_s^2}{2(P_s + 7P_0)} \quad (3.3)$$

where

- $P_{so}$  is peak static (side-on) overpressure
- $P_0$  is ambient air pressure in an undisturbed medium
- $\rho_0$  is density of air ambient pressure ahead of the blast wave
- $a_0$  is the speed of sound in air at ambient pressure



### 3.1.2.1 The ideal shock wave

An explosion in air is often accompanied by a very rapid rise in pressure and the formation of a shock wave as described in Section 3.1. The shape of the pressure depends of the type of explosion; it differs between gas and nuclear explosions and for high explosive explosions. After the shock wave has propagated some distance, the shock wave reaches a constant limiting velocity which is greater than the velocity of sound in air, or in the unburned gas in the case of a vapour cloud. [34]

An idealized representation of the blast wave is given in Figure 3.4.

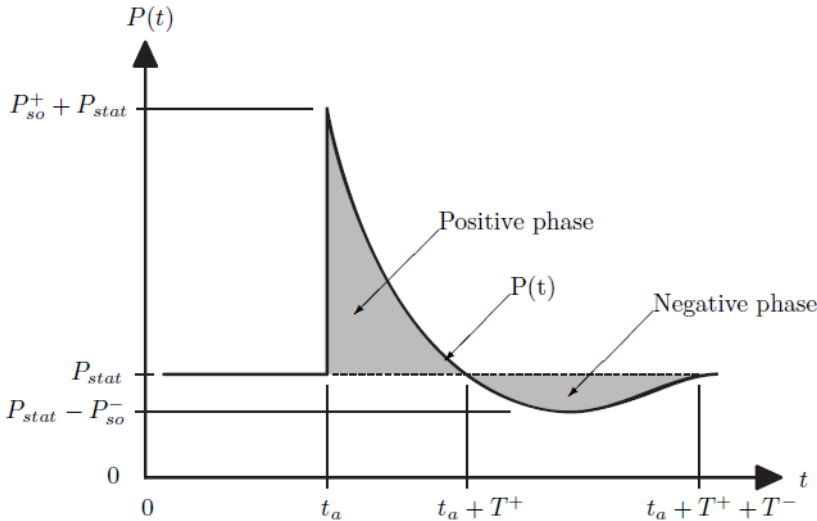


**Figure 3.4:** Idealized blast wave [32].

At arrival time  $t_a$ , the pressure rises quite abruptly to a peak value  $P_{so}^+ + P_0$  ( $P_{stat}$  in Figure 3.4 and Figure 3.5) for detonations with high

explosives. The pressure then decays to an ambient pressure at time  $t_a + T^+$ , before it drops to a partial vacuum of amplitude  $P_{so-}$  and eventually returns to  $P_0$  at total time  $t_a + T_+ + T_-$ . The quantity  $P_{so+}$  is usually peak side-on overpressure. This is the pressure that occurs at the side of the structure being passed by a blast wave. [34]

The time history above the initial ambient pressure is called the positive phase, of duration  $T^+$ , and the negative phase is the portion below  $P_0$ , of amplitude  $P_{so-}$  and duration  $T^-$ . A widely used equation for describing the positive phase of the overpressure decay curve is the modified Friedlander equation. [34]

$$P(t) = P_0 + P_{so} + (1 - t/T^+)e^{-bt/T^+} \quad (3.4)$$

where  $b$  is a decay coefficient of the the Friedlander curve.

The accumulated impulse is simply the integral of the pressure curve during the positive phase and the negative phase respectively:

$$I_s^+ = \int_{t_a}^{t_a+T^+} [P(t) - P_0] dt \quad (3.5)$$

$$I_s^- = \int_{t_0+T^+}^{t_a+T^++T^-} [P_0 - P(t)] dt \quad (3.6)$$

### 3.1.2.2 Reflected shock wave

The properties of air blast waves as they propagate freely through air, are seriously increased in value as they reflect from an object and diffract around it. When the shock wave hits a structure the conditions immediately behind the shock front are as described earlier in section 3.1.2. When the front hits a rigid structure it is reflected, the incident particle velocity become zero and the pressure, density and

## CHAPTER 3. THEORY

temperature are all increased above the values in the incident wave. The overpressure at the wall surface is the reflected overpressure  $P_r$ .

For low values of side-on pressure, the reflected pressure approaches the acoustic limit of twice the incident overpressure,  $P_r = 2P_{so}$ . For strong shocks an upper limit often cited in the literature is  $P_r = 8P_{so}$ . This limit does not take into account that air ionizes and dissociates, it behaves as a perfect gas at the high pressures and temperatures. If real gas effects was considered this limit can be much greater as proved by Doering and Burkhardt, and Shear and McCane. [32]

The shock front parameter were first introduced in [35] and derived from the considerations of conservation of momentum and energy. All equations are given under the assumption that air behaves as a perfect gas with specific heat ratio  $\gamma$  and that the particle velocity is equal to zero ahead of the shock front [34].

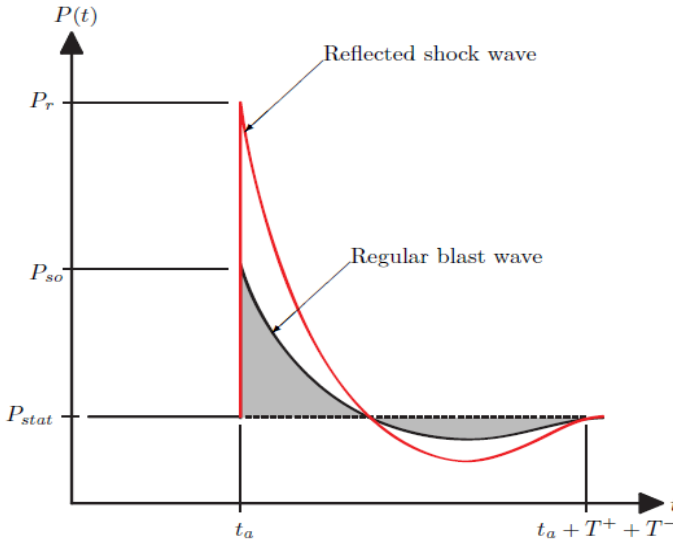


**Figure 3.5:** Reflected pressure side-on pressure [2].

The peak reflected over pressure  $P_r$ , which occurs if the blast wave strikes a flat surface at normal incidence, is given by

$$P_r = 2P_{so} + (\gamma + 1)q_s \quad (3.7)$$

where the dynamic pressure  $q_s$  is given as

$$q_s = \frac{1}{2}\rho_s u_s^2 \quad (3.8)$$

and the particle velocity  $u$  behind the wave front is

$$u = \frac{a_0 P_{so}}{\gamma P_0} + \left(1 + \frac{\gamma + 1}{2\gamma} \frac{P_{so}}{P_0}\right)^{-1/2} \quad (3.9)$$

$\gamma$  is the specific heat ratio  $C_p/C_v$ . Then substituting Eq.(3.8) and Eq.(3.9) into Eq.(3.7) and setting  $\gamma = 1.4$ , rearrangement give the reflected pressure

$$P_r = 2P_{so} \left( \frac{7P_0 + 4P_{so}}{7P_0 + P_{so}} \right) \quad (3.10)$$

### 3.1.3 Failure modes

For plates subjected to blast loading, the event of failure are classified into three different modes [6] :



(a) Failure Mode I



(b) Failure Mode II



(c) Failure Mode III

**Figure 3.6:** Failure modes for clamped plates subjected to blast load [6].

The failure modes in Figure 3.6 are described as

- Mode I: Large ductile deformation.
- Mode II: Partial tensile tearing.
- Mode III: Transverse shear.

Failure mode II have two subcategories

- Mode IIa: Complete tensile tearing with increasing deformation.

- Mode IIb: Complete tensile tearing with decreasing deformation.

Mode II, complete tensile tearing of the plate, have two sub modes. While Mode II is the borderline case between Mode I and Mode IIa. Mode IIb is the borderline case between Mode IIa and Mode III [36]. The first mode occurs with the lowest impulse and so on with increasing impulse [6].

## 3.2 Numerical methods

### 3.2.1 Lagrangian and Eulerian FEA

One of the most widely used formulations in classical solid mechanics is the Lagrangian FEA. The great strength of the Lagrangian formulation roots in the ability to describe complicated boundary conditions and to deal with Cartesian, cylindrical, spherical and any other coordinate systems with ease.

In Lagrangian meshes, the nodes and elements move with the material. Boundaries and interfaces remain coincident with the element edges, while the quadrature points also move with the material, resulting in the constitutive equations always being evaluated at the same material point. This is advantageous for history dependent materials. Lagrangian elements are limited by the elements capability to deal with large element distortions.

In the Lagrangian approach all physical quantities are expressed as a function of time and their initial position  $\mathbf{X}$ . Each node of the mesh remains coincident with a material point as seen in Figure 3.7.

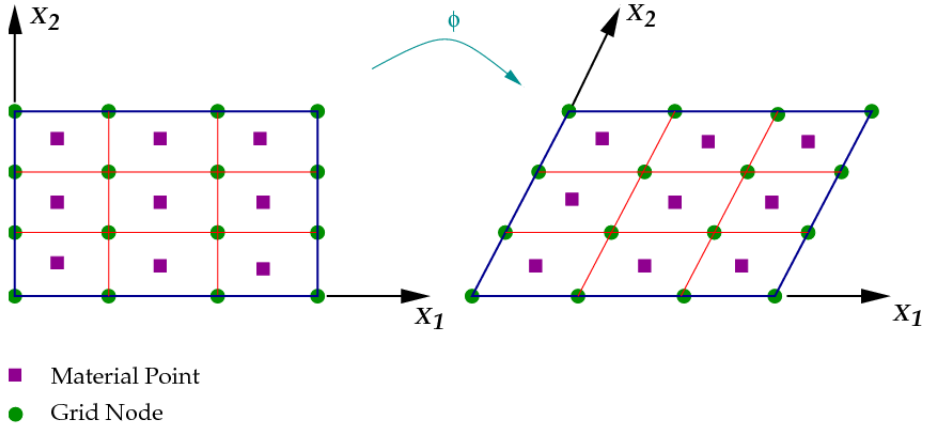


**Figure 3.7:** Lagrangian mesh transform [37].

In the Total Lagrangian formulation, strain and stress measures are referred to the initial (undeformed) configuration  $C_0$ . Alternatively to the Total Lagrangian formulation is the Updated Lagrangian formulation, where a known deformed configuration  $C_n$  is taken as the initial state and continuously updated as the calculation proceeds. Although these formulations are superficially quite different, the underlying mechanics of the two formulations are identical. Furthermore, expressions in the total Lagrangian formulation can be transformed to updated Lagrangian expressions and vice versa. [38]

Until recently, Eulerian meshes have not been applied in solid mechanics. Eulerian meshes are most appealing in problems with large deformation. The Eulerian elements do not deform with the material, so for problems with large distortions, the elements remain at their original shape, see Figure 3.8. In the Eulerian approach they are functions of time and their current position.

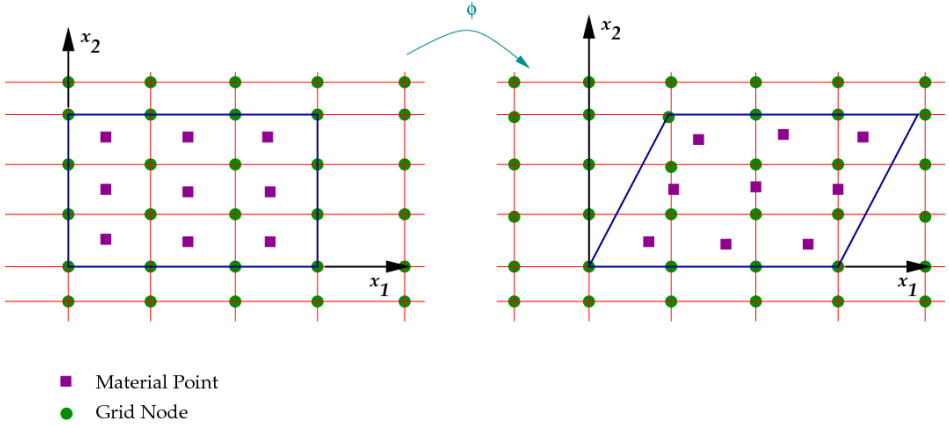


**Figure 3.8:** Eulerian mesh transform [37].

Widely used is Eulerian- Lagrangian methods for fully coupled analysis with large deformations, where the Eulerian mesh is mapped onto the Lagrangian mesh. This is very time consuming and computational expensive. The motivation for this thesis is to further examine the advantages and accuracy of applying kinetic molecular theory rather than Arbitrary Lagrangian-Eulerian (ALE) formulations. Most simulation will be performed in the discrete particle method based solver Impetus-Afea, hence it is chosen to omit theory regarding ALE. It is referred to [38] and [39] for further deriving of ALE and FSI theory, respectively.

### 3.2.2 Explicit time integration

For short duration loads such as impact, explicit time integration methods are best suited. In explicit methods equation solving is not necessary, but they are conditionally stable. There is a critical time step that must not be exceeded if the numerical process is not to "blow up" and becoming unstable. This results in the number of time



steps acquired being rather large, but computational costs per step is low. The central difference method is widely used in explicit methods in computational mechanics and physics. For explicit methods, the displacement at time  $t_{n+1}$ ,  $D_{n+1}$ , is obtained directly (explicitly) from the equilibrium equation conditions at one or more preceding time steps ( $t < t_n$ ) without solving an equation system. This makes explicit methods computational inexpensive. [40]

An algorithm with a variable time step is necessary since the stable time step changes as the mesh deforms and the wave speed changes due to the stress. The time increment is defined by [38].

$$\Delta t^{n+1/2} = t^{n+1} - t^n, \quad t^{n+1/2} = \frac{1}{2}(t^{n+1} + t^n), \quad \Delta t^n = t^{n+1/2} - t^{n-1/2} \quad (3.11)$$

The central difference formula for velocity is where the definition of  $\Delta t_{n+1}$  is used as

$$\dot{d}^{n+1/2} \equiv v^{n+1/2} = \frac{d^{n+1} - d^n}{t^{n+1} - t^n} = \frac{1}{\Delta t^{n+1/2}}(d^{n+1} - d^n) \quad (3.12)$$

The acceleration can be expressed directly in terms of displacement:

$$\ddot{d}^n \equiv a^n = \frac{\Delta t^{n-1/2}(d^{n+1} - d^n) - \Delta t^{n+1/2}(d^n - d^{n-1})}{\Delta t^{n+1/2} \Delta t^n \Delta t^{n-1/2}} \quad (3.13)$$

It is desirable to include stiffness- proportional damping  $\mathbf{C} = \beta \mathbf{K}$  in order to damp high-frequency numerical noise. This is causing the effective stiffness,  $\mathbf{K}^{\text{eff}}$ , becoming non-diagonal and equation solving is required. This problem may be overcome and equation solving avoided if only a half time step is taken.

For equal time steps, Eq. (3.13) reduces to the central difference formula for second derivatives of a function given as

$$\ddot{d}^n \equiv a^n = \frac{d^{n+1} - 2d^n + d^{n-1}}{(\Delta t^n)^2} \quad (3.14)$$

The equation of motion with time integration at time step  $n$  becomes

$$Ma^n = f^n = f^{ext}(d^n, t^n) - f^{int}(d^n, t^n) \quad (3.15)$$

It is noted that the mass matrix is constant for a Lagrangian mesh.

### 3.2.2.1 Stability of the Explicit Time integration

For rate-dependent materials the time step size of an explicit calculation changes from time step to time step due to the change in element length when the element is distorted. The efficiency of the explicit method depends on taking the maximum possible time step size. It is still critical that the time step size is conservative since because explicit methods can not retake a time step if the solution starts to diverge, because only one time state is stored. The time step size given in Eq.3.16. A safety factor,  $s_f$ , typically between 0.25 to 0.5, is commonly used for problems involving explosives, are to guarantee that the time step is conservative.

$$\Delta t \leq s_f \frac{2}{\omega} (\sqrt{\xi^2 + 1} - \xi) \quad (3.16)$$

The time step function is of elastic properties and the mesh geometry. In an elastoplastic material, the plastic hardening slope is typically orders of magnitude less than the elastic moduli. Using plastic moduli for the time step estimation gives a time step size larger than the elastic one by the square root of the ratio of the elastic to plastic moduli. By increasing the time step size by two or more orders of

magnitude would be very attractive. However, the stability will be lost if the material unloads elastically. The time step is therefore always estimated using the elastic properties. [41]

If the time steps exceeds the critical value,  $\Delta t_{cr}$ , the solution will grow unboundedly. For linear problems, instability issues lead to exponential growth of the solution and cannot be overlooked. For non-linear problems such arrested instabilities can lead to a large overprediction of displacements, although they are not detectable by pursuing the results. By performing an energy balance check, it is possible to monitor if there is any violation of the conservation of energy. [38]

### 3.2.2.2 Time Integration in Abaqus/Explicit

Abaqus/Explicit uses a central difference rule to integrate the equations of motion explicitly through time using kinematic conditions at one increment to calculate the kinematic conditions at the next increment [9]. Abaqus/ Explicit solves for dynamic equilibrium at each time step, which states that the nodal mass matrix  $\mathbf{M}$ , times the nodal accelerations  $\ddot{u}$ , equals the net nodal forces. The following deriving of the explicit relations applied in Abaqus/ Explicit are from [9].

For explicit methods lumped mass is applied. The mass matrix is diagonal and the acceleration of any node is determined completely by its mass and the net force acting on it. There are no simultaneous equations to solve which make the equation solving inexpensive, but the time steps needed are large.

The half-steps method are implemented in Abaqus/Explicit. The accelerations are integrated through time using the central difference

rule, which calculates the change in velocity assuming the acceleration is constant. The change in velocity is added to the velocity from the previous time step which is at the midpoint of the previous time interval:

$$\dot{u}_{t+\frac{\Delta t}{2}} = \dot{u}_{t-\frac{\Delta t}{2}} + \frac{\Delta t_{t+\Delta t} + \Delta t_t}{2} \ddot{u}_t \quad (3.17)$$

The velocities are integrated through time and added to the displacements at the beginning of the time increment. The displacement at the end of the time increment is then obtained:

$$u_{t+\Delta t} = u_t + \Delta t_{t+\Delta t} \dot{u}_{t+\frac{\Delta t}{2}} \quad (3.18)$$

The element calculations include determining elements strains and applying the material constitutive relationships to determine the element stresses and internal forces acting on the nodes. The element calculations may be given in a short summary:

- a. Element strain increments,  $\Delta \varepsilon$ , are computed from the strain rate  $\varepsilon$ .
- b. The stress,  $\sigma$ , are computed from constitutive equations;

$$\sigma_{t+\Delta t} = f(\sigma_t, \Delta \varepsilon) \quad (3.19)$$

- c. internal nodal forces are assembled;  $\mathbf{I}_{t+\Delta t}$

The time is then equal to  $t + \Delta t$  and the steps is repeated.

### 3.2.3 Kinetic molecular theory

Until recent, continuum-based ALE approaches have been considered the most accurate tool for simulating fully coupled Lagrangian-Eulerian analysis.

## CHAPTER 3. THEORY

---

The corpuscular method, also known as the discrete particle method is based on the theory first introduced by Bernoulli in 1738 and involves the study of gas molecules and their interactions on microscopic level. Maxwell developed this theory from its origin to allow for numerical treatment of gas volumes at macroscopical level. The following relations are from the derival of the corpuscular method performed in [25].

The theory is based on the following assumptions

- The average distance between the molecules is large compared to their size.
- There is a thermo-dynamical equilibrium, i.e. the molecules are in random motion.
- The molecules obey Newton's law of motion.
- The molecule-molecule and molecule-structure interactions are perfectly elastic collisions.

In 1860 Maxwell derived a very elegant expression from Bernoulli's kinetic molecular theory for the molecular velocity distribution at thermal equilibrium

$$f(v) = 4\pi \left( \frac{M}{2\pi RT} \right)^{3/2} v^2 \exp\left( \frac{-Mv^2}{2RT} \right) \quad (3.20)$$

where

$f(v)$  is the probability density function from the molecular velocity

$M$  is the molar mass,  $R$  is the universal gas constant

$T$  is the temperature

The root-mean-square velocity for a molecule may be found as:

$$v_{rms} = \sqrt{\int_0^\infty v^2 f(v) dv} = \sqrt{\frac{3RT}{M}} \quad (3.21)$$

From these statistical descriptions, it is possible to derive the mean-free-path of the particles,  $\lambda$ , and the frequency of collision. In blast mechanics, it is important to describe the pressure accurately. By applying the kinetic molecular theory, the total pressure acting on a surface may be calculated.

Assume one single molecule with mass  $m_i$  and velocity  $v = [v_{x,i}, v_{y,i}, v_{z,i}]^T$  is located inside a rectangular box with side lengths  $L_x, L_y$  and  $L_z$ , see Figure 3.9.

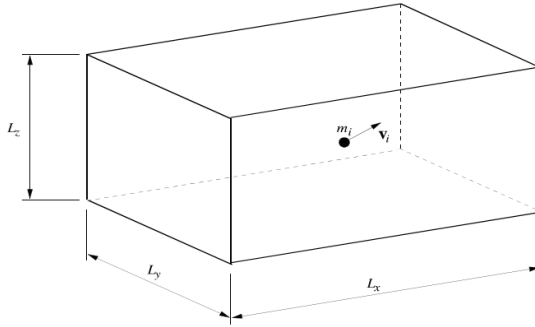


**Figure 3.9:** Particle moving around in box [25].

The frequency at which the molecule will impact with the wall of the

box in positive x-direction becomes

$$f = \frac{v_{x,i}}{2L_x} \quad (3.22)$$

Since it is assumed that the collision is perfectly elastic, the transferred impulse at each impact is

$$j_{x,i} = 2m_i|v_{x,i}| \quad (3.23)$$

The total impulse transferred to the wall of the box becomes

$$J_{x,i} = f j_{x,i} t = \frac{m_i v_{x,i}^2 t}{L_x} \quad (3.24)$$

Hence the average pressure against the wall

$$p_{x,i} = \frac{J_{x,i}}{At} = \frac{m_i v_{x,i}^2}{V} \quad (3.25)$$

Having N molecules the pressure becomes

$$P_y = P_z = P_x = \frac{1}{V} \sum_{i=1}^N m_i v_{x,i}^2 \quad (3.26)$$

At thermal equilibrium the kinetic energy will be evenly distributed between the different Cartesian directions. The velocity in each direction are then equal to  $\frac{1}{3}\bar{v}^2$ . Substituting this velocity into Eq. (3.26) the pressure becomes

$$P = P_x = P_y = P_z = P_x = \frac{1}{V} \sum_{i=1}^N m_i v_{x,i}^2 = \frac{1}{3V} m \bar{v}^2 = \frac{2W_k}{3V} = \frac{2}{3} w_k \quad (3.27)$$

where

$m$  is the total mass of the molecules

$W_k$  is the total translational kinetic energy of the particles

$w_k$  is the specific translational kinetic energy

For a mono-atomic gas  $w_k$  is equivalent to the total specific energy  $e$ , as virtually no energy is stored as molecular spin or vibrations.

The pressure in ideal gas with constant heat capacities can be expressed as

$$p = \left( \frac{C_p}{C_v} - 1 \right) e \quad (3.28)$$

In attempt to match the high explosive pressure-volume relationship as accurately as possible,  $\gamma$  should be set equal to 5/3 which is the largest value feasible [26].

Maxwell further managed to bring more understanding to details about the molecular interaction in an ideal gas. From his statistical descriptions, the quantities such as the mean-free-path of a particle,  $I$ , may be derived:

$$I = \frac{I}{\sqrt{2} \pi n r_p^2} \quad (3.29)$$

and the frequency of collision,  $f_c$

$$f_c = n r_p^2 \sqrt{\frac{8 \pi R T}{M}} \quad (3.30)$$

where  $r_p$  is the molecular radius and  $n$  is the number of molecules per unit volume.

It is not possible to model every single molecule in a full scale blast scenario and thus are the system reduced from many molecules to



fewer and larger particles. Depending on the molecular weight, the number of molecules may be in the order of  $10^{22} - 10^{23}$  for each gram detonation product. The need for computational efficiency in the numerical implementation has led to the following assumptions and deviations from the kinetic gas theory: [26]

- The particles are rigid and they are given a spherical shape
- Each particle represent many molecules, typically  $10^{15} - 10^{20}$  depending on the application.
- For each individual particle there is a balance between translational energy  $W_t$ , and spin/vibration energy  $W_s$ . This balance is determined directly from  $\gamma = C_p/C_v$ , where  $C_p$  and  $C_v$  are the heat capacities at constant pressure and volume, respectively.
- To obtain a smoother pressure distribution the impulse transfer from particle-fabric collisions is slightly smeared out in time.

It has further been observed that using the corpuscular method is less time consuming and gives as accurate results compared to current state-of-the-art continuum-based approaches to fully coupled blast simulations. Limitations that apply to the method in its current form: It is based on an ideal gas assumption that deviates from the equations-of-state that usually are applied when describing a blast load. The method is dispersive, which means that elastic waves are quickly smeared out. The dispersion is caused by a particle mean-free-path that is several orders of magnitude larger than the molecular mean-free-path in real gas. [25]

There are three main motivations for using the kinetic molecular approach. Firstly, the method is based on a Lagrangian description of motion where advection related errors are not an issue, in contrast to to arbitrary Lagrangian- Eulerian methods. Second, the interaction between air, high explosives and structural parts are allowed to be represented in a simple, physically clear and robust manner. Finally, the kinetic molecular theory can be combined with finite elements for

studying fully coupled structural responses.

### 3.3 Constitutive model

In this thesis, a thermoelastic-thermoviscoplastic constitutive model described in [42] is applied in the numerical simulations. The computational model includes linear thermoelasticity and viscoelasticity and is developed for isotropic materials. Fracture was not an issue during the experiments at Østøya, hence a fracture criteria is therefore not covered.

The three essential components of elastic-plastic analysis is the yield criterion, flow rule and hardening rule. The yield criterion relates the state of stress to the onset of yielding. The flow rule relates the state of stress to the corresponding six increments of plastic strain when an increment of plastic flow occurs [43]. In general when the material work-harden, the strength is increased. The hardening rule describe the evolution of the yield surface as material is deform plastically.

The yield function in the presence of isotropic hardening is expressed as

$$f(\boldsymbol{\sigma}, R) = \phi(\boldsymbol{\sigma}) - \sigma_Y(R) \leq 0 \quad (3.31)$$

where

$\sigma_{eq} = \phi(\boldsymbol{\sigma})$  is the equivalent stress

$\sigma_Y = \sigma_0 + R$  is the flow stress

$\sigma_0$  is the initial yield stress

As the material is plastically deformed, the isotropic hardening variable  $R$  and thus the flow stress  $\sigma_Y$  are both increasing, and as a result

## CHAPTER 3. THEORY

---

the elastic regions is enlarged in stress space.

The strain increments are composed of an elastic, plastic and a thermal part;

$$d\boldsymbol{\varepsilon} = d\boldsymbol{\varepsilon}^e + d\boldsymbol{\varepsilon}^p + d\boldsymbol{\varepsilon}^t \quad (3.32)$$

The elastic rate-of-deformation tensor  $d\boldsymbol{\varepsilon}^e$  is defined by

$$d\boldsymbol{\varepsilon}^e = \frac{1 + \nu}{E} \boldsymbol{\sigma}^{\Delta J} - \frac{\nu}{E} \text{tr}(\boldsymbol{\sigma}^{\Delta J}) \mathbf{I} \quad (3.33)$$

where

$E$  and  $\nu$  are elastic constants

$\mathbf{I}$  is second order unit tensor

$\boldsymbol{\sigma}^{\Delta J}$  is Jaumann rate of Cauchy stress tensor  $\boldsymbol{\sigma}$

The thermal rate-of-deformation  $d\boldsymbol{\varepsilon}^t$  is defined by

$$d\boldsymbol{\varepsilon}^t = \alpha \dot{T} \mathbf{I} \quad (3.34)$$

where  $\dot{T}$  is the rate of temperature and  $\alpha$  is linear thermal expansion coefficient.

The plastic rate-of-deformation tensor  $d\boldsymbol{\varepsilon}$  is defined by the associated flow rule

$$d\boldsymbol{\varepsilon} = \dot{p} \frac{\partial f}{\partial \boldsymbol{\sigma}} = \frac{3}{2} \dot{p} \frac{\boldsymbol{\sigma}'}{\sigma_{eq}} \quad (3.35)$$

where  $\dot{p}$  is the equivalent plastic strain rate.

The von Mises yield function with the presence of isotropic hardening  $R$ , is expressed as

$$f(\boldsymbol{\sigma}, R, T) = \sigma_{eq}(\boldsymbol{\sigma}) - \sigma_Y(\sigma_0, R) = \sigma_{eq}(\boldsymbol{\sigma}) - (\sigma_0 + R(p, T)) \quad (3.36)$$

The equivalent stress  $\sigma_{eq}$  is given by the von Mises yield criterion as

$$\sigma_{eq} = \sqrt{\frac{3}{2} \boldsymbol{\sigma}' : \boldsymbol{\sigma}'} \quad (3.37)$$

A widely used and purely empirical material model that accommodates for large strains, high strain-rates and temperature softening is the Johnson and Cook constitutive model. This constitutive relation has a multiplicative formulation given by

$$\sigma_{eq} = [A + Bp^n][(1 + C \ln \dot{p}^*)][1 - T^{*m}] \quad (3.38)$$

$A, B, C, n, m$  material constants

$T^* = \frac{T - T_0}{T_m - T_0}$  is the homologous temperature

$(T_0, T_m)$  are the room and melting temperature of the material

$\dot{p}^* = \frac{\dot{p}}{\dot{p}_0}$  is a dimensionless strain rate

$\dot{p}_0$  is a user-defined strain rate

If the strain-rate is low, this constitutive relation of the Johnson-Cook model is not physical. To avoid the effects of low strain rates,

the constitutive relation is often modified in the following manner

$$\sigma_{eq} = [A + Bp^n][1 + \dot{p}^*]^C[1 - T^{*m}] \quad (3.39)$$

The non-linear isotropic hardening law is further used to represent the strain hardening [44]

$$\sigma = (\sigma_Y + \sum_{i=1}^2 Q_i(1 - \exp(-C_i\varepsilon)))(1 + \frac{\dot{\varepsilon}}{\dot{\varepsilon}_0})^q(1 - T^{*m}) \quad (3.40)$$

Evaluating the yielding in the viscoplastic domain ( $f > 0$ ), and combining Eq. (3.38) or Eq. (3.39) with Eq. (3.40) the plastic strain-rate of the material is achieved

$$\dot{p} = \begin{cases} 0 & \text{for } f \leq 0 \\ \dot{p}_0 [ (\frac{\sigma_{eq}(\sigma)}{\sigma_Y(\sigma_0, R, T)})^{1/c} - 1 ] & \text{for } f > 0 \end{cases}$$

### 3.4 Digital Image Correlation

Digital Image Correlation (DIC) is a numerical post-processing technique which uses recorded digital images from mechanical experiments, to obtain measurements of both displacement and strain fields of a particular specimen surface.

In this thesis, three dimensional DIC is used to measure the out of plane deformations of the steel plates subjected to blast load.

In the DIC algorithm, the grey scale at deformed stage (current configuration) is compared to the grey values of the specimen at a initial stage (reference configuration). The deformation of the specimen from the reference to the current stage, in the two-dimensional image

coordinate system, may be described by a set of parameters. These parameters are then calculated in an optimization algorithm, minimizing the differences in grey scale values between the reference and the current configuration.

The image correlation technique aims to minimize the squared difference in grey scale values within a rectangular region of an image (subset), and is defined by the correlation function  $F$  [45]

$$F = \text{sum}(I_r(X_r) - I_C(x_i))^2 \quad (3.41)$$

where

$i$  denotes a specific pixel

$I_r$  is the reference image

$I_c$  is the current image

The DIC software developed at SFI SIMLab, employ Newton-Raphson iteration methods as mathematical formulation and the correlation function  $F$  is used as an objective function in the Newton-Raphson optimization.

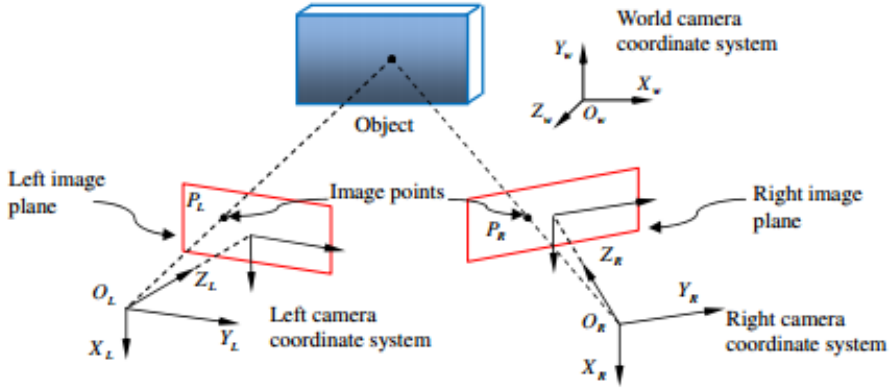


**Figure 3.10:** Schematic drawing recovering the three-dimensional structure of an object using two imaging sensors [46].

3D-DIC can measure all three components of displacement of the test object. The small amounts of out of plane motion of an object occurred during the loading, can be accurately detected without affecting the accuracy of the other two in-plane displacement components [47].

The comparison between the images can either be performed on a small subset of pixels or on a finite element mesh. Using the latter approach, the correlation problem is formulated as a (global) finite element mesh of Q4 elements. Instead of applying individual optimization of subsets, the correlation is carried out as a global optimization on a mesh of elements. Also, instead of optimizing the displacement of the center point and the displacement gradient of the subset, the nodal displacements in the mesh is optimized.

The DIC- approach requires high speed cameras which have to be calibrated prior to the image recordings. A powerful light source is

also preferable to light up the plate. A random speckle pattern is applied by spray painting the surface of the specimen with black and white paint.

The DIC technique has in recent years become a well established tool for measuring strain and displacements for a wide range of materials [47].

### 3.5 ConWep

The widely used blast load standard Conventional Weapons Effects Program (ConWep) is developed by the U.S. Defence. The expected peak pressure, impulse and duration of the shock wave are estimated by applying stand-off distance and TNT equivalent mass in the program. ConWep is based on extensive experimental work by Kingery and Bulmash [48]. The experimental data is given in Appendix A, where it is observed that for shorter stand-off distances the estimated blast parameters are not as accurate as for the increasing stand-off distances.

The drawback with the loads from standards like ConWep are that it is impossible to achieve the exact same conditions as during the experiments the standard is based on.



# Chapter 4

## Material

### 4.1 Docol 600 DL Steel

In order to get reliable results in the numerical simulations, material testing should be performed for the material in use.

The Docol 600DL is a cold-rolled, low-strength and high-hardening steel produced by SSAB in Sweden. During manufacturing the steel is subjected to a heat treatment which results in a dual-phase structure of ferrite and martensite. The ferrite gives the formability to the steel, while the martensite gives the strength [36].

The chemical composition of the dual-phase Docol 600 DL is given in Table 4.1.

**Table 4.1:** Chemical composition of Docol 600DL [44]

C%	Si%	Mn%	P%	S%	Al%
0.10	0.40	1.50	0.010	0.002	0.040

## 4.2 Calibration of Docol 600 DL

When dealing with problems with high velocity impact and impulse loading, the material behaviour is often described with a viscoplastic material model. The Johnson-Cook material model describes materials subjected to large deformations, high strain rates and high temperature well. Based on the work conducted in [44] the Docol 600 DL does not display much anisotropy and the J2 flow theory is suitable to describe the plastic material behaviour.

In previous work by [44] and [36] the diversity in yield- and ultimate strength for the different material thickness' are given between 280 MPa and 370 MPa to 600 MPa to 700 MPa, respectively. This demonstrates the importance of material testing of the respective material in use and correct calibration of the results, considering the diversity in parameters obtained. The nominal elastic properties are described by a Youngs modulus of 210 GPa and a Poisson's ratio of 0.33.

The material used in this thesis is 0.8 mm Docol 600 DL and a material test using the respective thickness have been performed. The main focus of this thesis is numerical simulations of the dynamic blast response of a plate and only a recalibration of a previous uniaxial tension test by Holmen [49] is performed.

### 4.2.1 Stresses and strains

The following relations are applied in the calibration of the material parameters using the stress and strain recorded by the extensometer [50].

Engineering strain

$$\varepsilon_e = \frac{L - L_0}{L_0} = \frac{\Delta L}{L_0} \quad (4.1)$$

Engineering stress

$$\sigma = \frac{F}{A_0} \quad (4.2)$$

Engineering plastic strain

$$\varepsilon = \varepsilon_e - \varepsilon_e^e = \varepsilon_e - \frac{\sigma_e}{E} \quad (4.3)$$

Correction of the engineering,  $\sigma_e - \varepsilon_e$ , curve due to stiffness in the extensometer

$$\varepsilon = (\varepsilon_{me} - \Delta\varepsilon_e) - \left( \frac{E_{corr} - E_{meas}}{E_{corr}E_{meas}} \right) \sigma_e \quad (4.4)$$

where  $E_{meas}$  is the calculated modulus of elasticity from the elastic part of the engineering stress-strain curve and  $E_{corr}$  is the correct value (i.e. 210000 GPa).

Relation between engineering and logarithmic strain

$$\varepsilon_l = \ln(1 + \varepsilon_e) \quad (4.5)$$

Relation between engineering and Cauchy (true) stress

$$\sigma_t = \sigma_e(1 + \varepsilon_e) \quad (4.6)$$

The logarithmic (true) plastic strain to failure is defined as

$$\varepsilon_l^p = \varepsilon_l - \frac{\sigma_t}{E} \quad (4.7)$$

### 4.2.2 Calibration employing extensometer values

The material parameters applied in the later numerical simulations are based on the calibration performed in this section. The measured modulus of elasticity  $E_{meas}$ , is calculated from the elastic part of the engineering  $\sigma_e - \varepsilon_e$  curve using 20 % and 80 % of  $\sigma_{0.2}$ . The  $\sigma_{0.2}$  yield stress is set to 365 MPa. The obtained value for  $E_{meas}$  is 191 [GPa]. It is noted that the calculated value of modulus of elasticity is not necessarily representing the real value.

To avoid damage on the extensometer during a tension test, the specimen is removed from the extensometer before fracture. To capture further post necking behaviour of the material, the plastic strain may be assumed according to the Voce hardening law. The pre-necking behaviour which is the primary hardening ( $Q_1$  and  $C_1$ ), saturates for small strains, while post necking is defined by the secondary hardening ( $Q_2$  and  $C_2$ ). The material strain rate sensitivity increases significantly after necking and appropriate values for  $C$  and  $\dot{\varepsilon}$  are set to 0.005 and 0.001 respectively, based on the work by [44].

As determined in the extensive work by Gruben in [44] adiabatic conditions are assumed and the temperature is set to zero, hence the temperature term in Voce law in Chapter 3.3 becomes equal to 1.

The post necking behaviour is assumed by extrapolating the  $\sigma - \varepsilon^p$  curve from the extensometer according to Voce hardening law. This

may cause considerable errors at large strains. Necking or localized deformation of ductile materials begins at the maximum load, where the increase in stress due to the decrease in cross-section area of the specimen, becomes greater than the increase in strain hardening in the material. After the necking process has started in the material, the strain rate increases significantly and delays further evolution of the neck. The strain-rate sensitivity term in the Johnson-Cook constitutive relation is thus included to capture this effect.

The material coefficients are obtained by fitting the  $\sigma - \varepsilon^p$  curve from the experiment to the assumed constitutive relation by using least squares method in Matlab, as seen in Figure 4.1. It is noted that the yield stress is also assumed according to Voce law. Table 4.2 give the achieved material parameters which are used in the later numerical simulations.

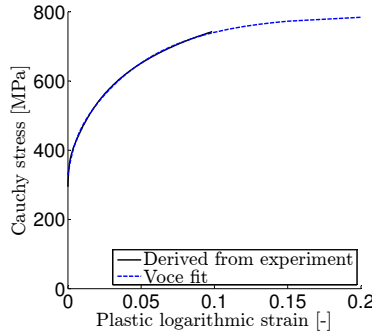


**Figure 4.1:** Stress- strain fit according to Voce law.

**Table 4.2:** Voce coefficients calibrated from extensometer values

$\sigma_0$ [MPa]	$Q_1$ [MPa]	$C_1$	$Q_2$ [MPa]	$C_2$	$\dot{\epsilon}$ [ $s^{-1}$ ]	C
327.7	384	20.41	78.93	245.1	0.001	0.005

A simulation of the uniaxial tension test using Abaqus/Explicit is performed with a 3D model of 1/4 of the test specimen. The material parameters given in Table 4.2 are used. The force-displacement curve from Abaqus/Explicit is compared to values recorded by the extensometer, see Figure 4.2.

The extensometer was removed at about 4 mm, hence the short extensometer curve.

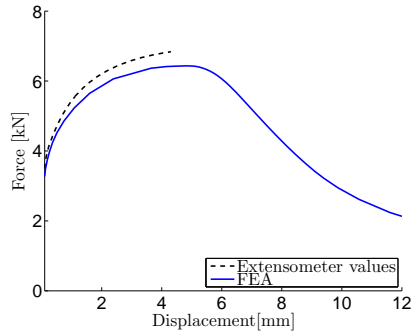


**Figure 4.2:** Extensometer values compared to tension test simulation in Abaqus/Explicit.

### 4.2.3 Calibration employing DIC values

The uniaxial tension test performed by [49] was also recorded with DIC and the stress-strain values retrieved. The DIC recordings in-

clude post-necking behaviour and Voce parameters have been optimized by [49] using LS-OPT. The final material coefficients from the DIC measure are given in Table 4.3.

**Table 4.3:** Voce coefficients [49]

$\sigma_0$ [MPa]	$Q_1$ [MPa]	$C_1$	$Q_2$ [MPa]	$C_2$	$\dot{\epsilon}$ [ $s^{-1}$ ]	C
370	236	39.3	408	4.5	0.001	0.005

The extrapolated post necking behaviour from the extensometer values and the DIC values are given for both material models in Figure 4.3, where the equivalent (Cauchy) stress is calculated from their respective material parameters.

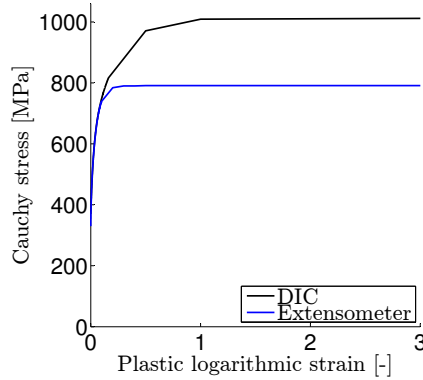


**Figure 4.3:** Voce fit for extensometer and DIC values.

The curve retrieved from DIC are approximately on top of the extensometer curve until necking. However, it is observed that the gradient

for the DIC values are increasing as the extensometer values levels off. The DIC measurements contain stress-strain history beyond necking and are able to describe this behaviour. While for the extensometer values, the post-necking behaviour is only assumed and does not display the correct behaviour of the material for large strains. The difference in fracture parameter is observed to be distinct.

The uniaxial tension test is also simulated using Abaqus/Explicit for the material parameters calibrated from DIC values.

The force- displacement curve from Abaqus/Explicit is compared to force-displacement curve obtained directly from the DIC program Ecorr, developed by [45]. As it is observed in Figure 4.4 the inclination of the curves fit, but the magnitude of the force does not coincide.

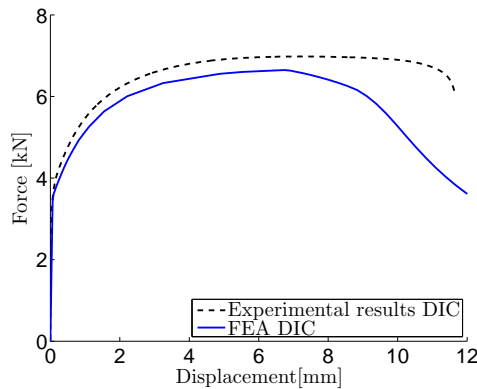


**Figure 4.4:** Experimental result from DIC compared to FEA with Voce fitted DIC values.

The force-displacement curves obtained in Abaqus/Explicit are compared for the two different material models below. The compliance between the two models is as expected sufficient until necking.



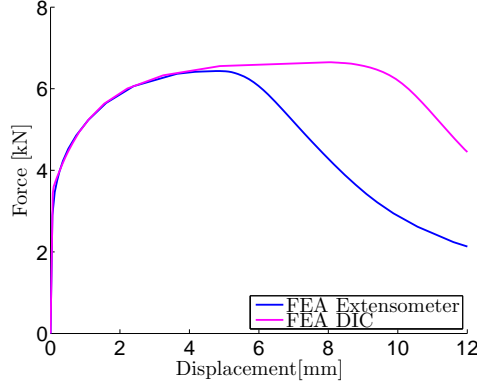


**Figure 4.5:** FEA Extensometer, FEA DIC and extensometer values.

In Figure 4.2 and Figure 4.4 the force-displacement obtained from Abaqus/Explicit does not coincide with the measured force-displacement curves from the extensometer and the DIC measure, respectively. The curves have the same inclination, but the numerical model underestimates the force for both material models. This is probably due to some modelling error in Abaqus/Explicit. The main motivation for this thesis is to investigate the accuracy of the discrete particle method compared to experimental results, thus further investigations of what is causing the numerical error is not performed. Due to the material parameters achieved being conservative, it is chosen to continue with these in the material model for the further numerical studies.

The material model based on the extensometer values, is used in the numerical simulations and a comparison for large strains between the two material models presented in this chapter, will be presented in chapter 7.



# Chapter 5

## Preliminary study

Before performing larger numerical simulations, the preferred element size should be determined and a foundation for comparing different numerical simulation codes should be established.

### 5.1 Mesh sensitivity study

To determine the element size for the later analysis, a mesh sensitivity study is performed in Abaqus/Explicit at stand-off distance 125 mm employing a pure Lagrangian formulation.

#### 5.1.1 Procedure

Due to symmetry conditions only a quarter of the steel plate is modelled in Abaqus/Explicit. The clamping frame is for simplicity reasons neglected in this preliminary study and the boundary is modelled

as fixed. Shell elements are employed due to its known accuracy in representing bending and low computational costs [43]. For shell elements, the element size has to be at least three times the thickness of the shell. Hence, the smallest element size is set to 2.5x2.5 mm. The charge consists of 30 g composition C4 and equivalent TNT mass is 38.4 g. Full integration is employed, hence hourglassing is not an issue [43].

The maximum permanent deflection is assumed to be lower in the preliminary analysis than in the experiments, as no slippage will occur at the boundaries. The material model is based on the data from Chapter 4.

For this simple problem, the applied load is based on ConWep, which is implemented in several numerical codes including Abaqus/Explicit. The pressure distribution is symmetrical and varies exponentially along the plate with maximum at the center. The intensity of the load varies with the distance from the detonation point, which is at the center of the plate (lower left corner in this model).

The analyses were performed with Abaqus/Explicit version 6.12 on a Dell Intel Core i7-2620M CPU personal laptop allocating 4 processors. See Appendix C.1 for keyword example.

### 5.1.2 Results

The sizes of the different elements and integration thickness' are given in Table 5.1 with corresponding computational time.

**Table 5.1:** Element size overview

Element size [mm]	# integration points through thickness	Max deflection [mm]	CPU time [h:min:s]
10	3	26.74	0:00:21
	5	27.00	0:00:24
	7	27.00	0:00:23
5	3	27.99	0:02:36
	5	27.61	0:02:49
	7	27.61	0:03:18
2.5	3	28.69	0:19:57
	5	27.79	0:22:01
	7	27.62	0:22:49

The displacement curves for the different element sizes and integration points shown is in Figure 5.2. It is observed that larger element sizes produce large oscillation, but the the permanent deflection is adequate for all element sizes. Employing less integration points seem to be more crucial for the permanent deflection, than the element size in this case. However, neither the element size nor the number of integration points influence the permanent deflection in particular, as the problem is rather straightforward.

The figure display the time-deflection history for the different element sizes (2.5 mm, 5 mm and 10 mm) and the for the different number of integration points chosen (3, 5 and 7).

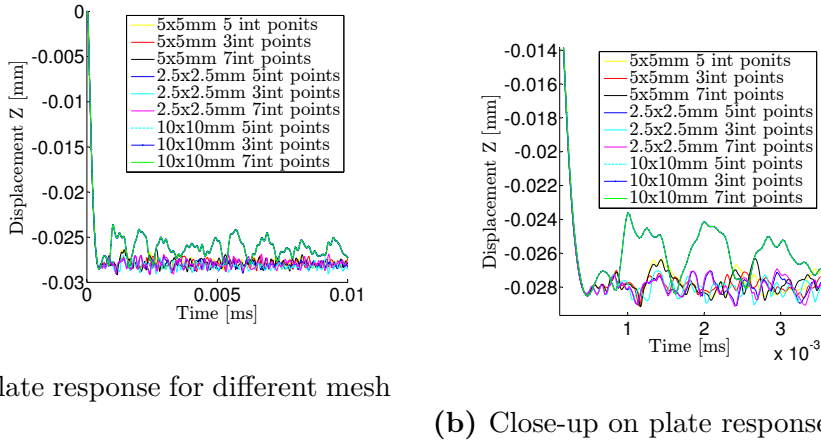


**Figure 5.1:** Comparison of element size and number of integration points.

For most problems, finer mesh increases the accuracy of the analysis, and the purpose of a mesh sensitivity study is to determine the most suitable element size for a certain degree of convergence. Based on the results shown in this section, 5x5 mm shell elements with 5 thickness integration points is chosen as the preferred mesh for the later analysis.

## 5.2 Comparison between Abaqus/Explicit and Impetus-Afea

In order to compare the accuracy between Abaqus/ Explicit and Impetus-Afea in the later numerical simulations, the plate response has been investigated for the simple problem given in Section 5.1. By employing the exact same geometry in both numerical codes, potential differences are easy to discover.

### 5.2.1 Procedure

The geometry in Impetus-Afea is modelled using a geometry box divided into different element sizes. The model consist of 1/4 of the target plate and with fixed boundary conditions as in Abaqus/Explicit. The charge geometry is 1/4 of a sphere.

Impetus-Afea does not employ the same set of shape functions as Abaqus/Explicit, thus it allows higher order elements to be employed without introducing any numerical noise present in numerical codes with non-linear elements present. Impetus-Afeas unique formulation, employs third order higher elements which have shown excellent performance for large strains in the previous work by [26] and [27]. It may be assumed that a single third order element in Impetus-Afea corresponds to three linear shell elements in Abaqus/Explicit [51]. As concluded in section 5.1.2, the 5x5 mm shell elements proved to be most efficient. The corresponding element size are 15x15x0.8 mm solid elements in Impetus-Afea.

Impetus utilizes a cubic 64-node hexahedron element formulation as seen in the Figure 5.2.

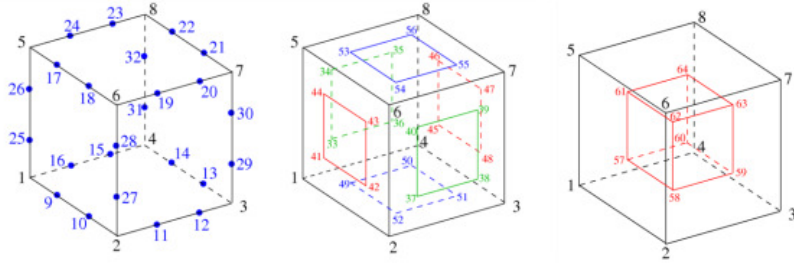


**Figure 5.2:** Element formulation [51].

In the previous simulation, the material values were tabulated into Abaqus/Explicit. To display a more accurate material behaviour, the SIMLab Metal Model have been utilized in these simulations, employing the material parameters from Section 4.2.2. These simulations are performed using a Xeon64 system Linux cluster allocating 4 processor. The computational time was low (i.e a few minutes), thus is not recorded.

### 5.2.2 Results

The time-deflection history is compared for two scenarios; stand-off distance 125 mm and 250 mm. The deflection and the blast impulse distribution along the plate for stand-off distance 125 mm, are given in Figure 5.3 and Figure 5.4 for Impetus-Afea and for Abaqus/Explicit in Figure 5.5.



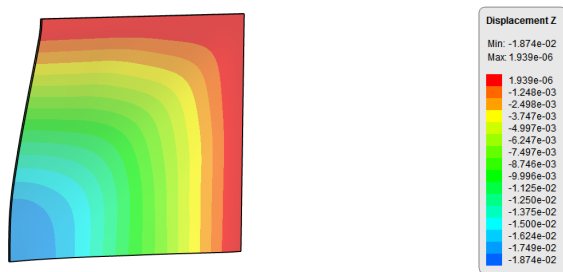


**Figure 5.3:** Displacement in loading direction from Impetus-Afea on a quarter plate.

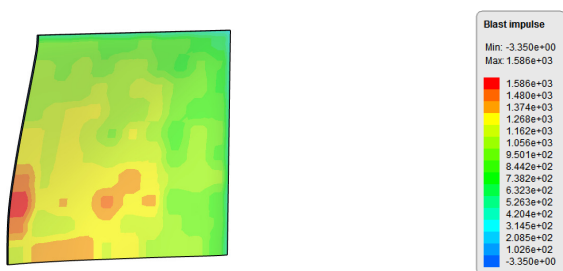


**Figure 5.4:** Blast impulse accumulated to the plate from Impetus-Afea on a quarter plate.

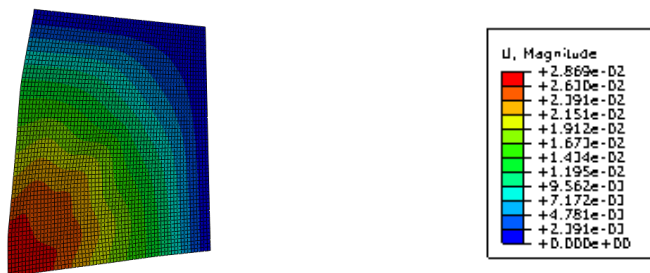


**Figure 5.5:** Permanent deflection from Abaqus/Explicit on a quarter plate.

The time-deflection history was examined for both scenarios for the center node of the plate. The results are quite different in proportions, but there are similarities between oscillations in the early time steps, as seen in Figure 5.6. As mentioned in section 3.2.3, the elastic waves are quickly smeared out in Impetus-Afea. This is due to the particle mean-free-path being several orders larger than the molecular mean-free-path in real gas. The elastic vibrations are therefore quickly damped out.

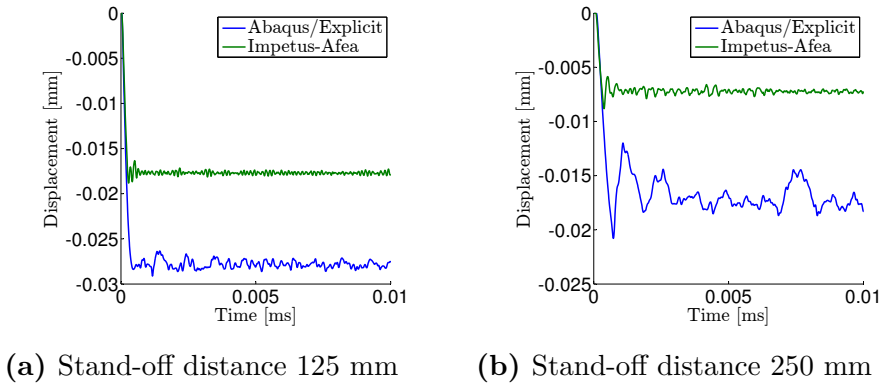


**Figure 5.6:** Time-deflection history for the two scenarios.

The difference in maximum and final deflection could be explained by the difference in element stiffness generated in the two numerical codes. When the explosive is located this close to the plate, the differences in load distribution between the two codes may influence the deflection significantly. Impetus-Afea is most suited for close range blasts [26], while the blast-load function based on ConWep imple-

mented in Abaqus/Explicit, is more accurate for blast with stand-off distance over approximately 500 mm, as mentioned in section 3.5.

The impulse applied at the center of the plates are given in Table 5.2.

**Table 5.2:** Accumulated impulse

	Abaqus/Explicit	Impetus-Afea
Impulse [kPams]	610.8	279.1

Abaqus/Explicit accumulate a larger impulse than Imeptus-Afea and this implies that there are great differences in the load distribution. Abaqus/Explicit distribute the blast wave symmetrically along the plate, while the load distribution are more random in Impetus-Afea. The different element formulation is also likely to produce diversity. The shell elements employed in Abaqus/Explicit display a softer behaviour than the higher order volume elements utilized in Impetus-Afea. It is expected that a more exact geometric model will improve the compliance between the two numerical codes and the differences in response are accepted in this preliminary study.

To compare the results between Abaqus/Explicit and Impetus-Afea with the experimental results, an analysis have been performed for stand-off distance 375 mm in Abaqus/Explicit. The plate response for all stand-off distances are given in Figure 5.7 and the permanent deflection in Table 5.3.

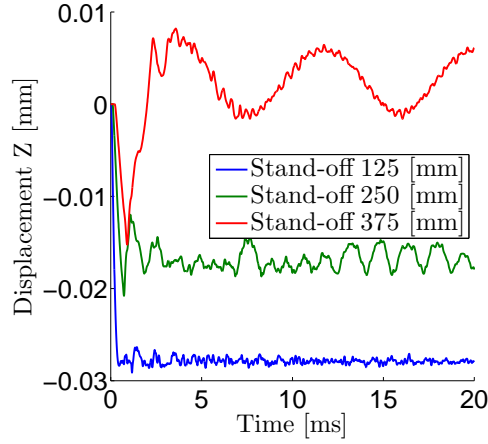
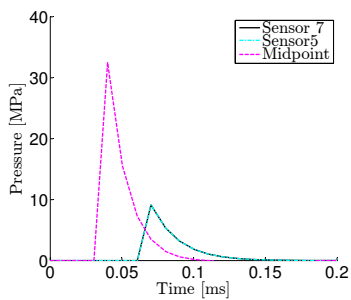


**Figure 5.7:** Permanent deflection from Abaqus/Explicit for all stand-off distance.

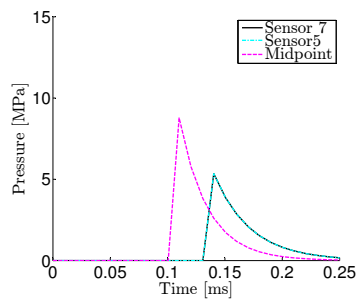
**Table 5.3:** Permanent deflection from the different stand-off distances

Stand-off distance [mm]	Deflection $\Delta Z$ [mm]
125	28.22
250	17.90
375	-6.03

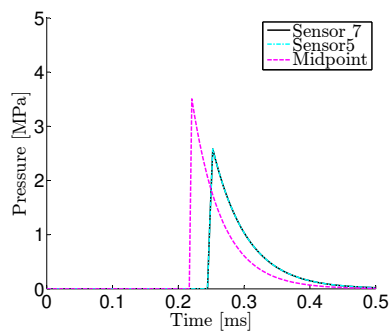
The load distribution from Abaqus/Explicit for the center of the plate, the boundary at top and boundary at side of the plate, are given in Figure 5.8.



(a) Stand-off 125 [mm]



(b) Stand-off 250 mm



(c) Stand-off 375 mm

**Figure 5.8:** Load distribution from ConWep.



# Chapter 6

## Experiments at Østøya

Free air explosion was performed on the 0.8 mm Docol 600 DL steel plates at Østøya, to verify the numerical simulations. This chapter presents the load distribution along the target plates and the plate response from the experiments.

### 6.1 Experimental set-up

The experiments were performed indoors in a concrete building at a closed military area at Østøya. The layout of the experimental set-up is shown in Figure 6.1. The steel plate (400 x 400 x 0.8 mm) was clamped with 16 pre-stressed M12-8.8 bolts to a rigid steel frame with dimensions 1000 x 1000 x 15 mm<sup>3</sup>. The steel frame has a square aperture, providing the specimen with a blast impact area of 300 x 300 mm<sup>2</sup>.

The explosive charge consisted of 30 g composition C4 with an (imperfect) spherical shape and diameter of 34.5 mm. The charge was positioned at various stand-off distances, i.e. 125 mm, 250 mm and

375 mm from the centre of the plate. The charge was held in place by a plummet as seen in the Figure 6.1c. The experiments were performed indoors with a large open door along the side of the concrete building.





(a) Frame and cameras



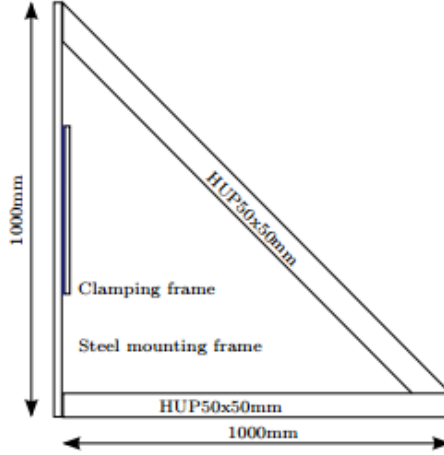
(b) Rigid frame



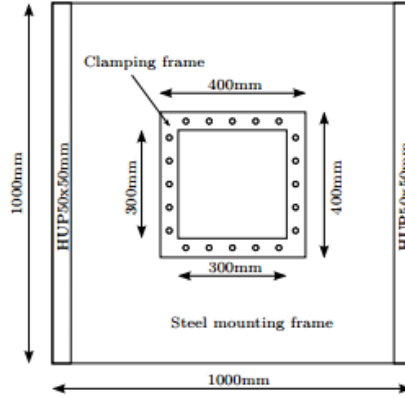
(c) Explosive charge

**Figure 6.1:** Experimental set-up.

The steel frame's dimensions are according to the drawings given in Figure 6.2. The frame was bolted to the concrete floor and is considered totally fixed.



(a) Side view of steel frame



(b) Front view of steel frame

**Figure 6.2:** Rigid steel frame

To measure the reflecting blast pressure, high pressure transducers (Kistler 603B) were mounted in the steel frame on each side of the plate. To capture the dynamic response of the plate, the Digital Image Correlation (DIC) technique was used. Two high-speed cameras were placed at a distance 3300 mm from the plate and a 3D displacement field of the plate was obtained. Figure 6.3 display the set-up of the cameras. A blast pencil was placed in between the two high-speed cameras to determine the time when the shock wave arrives at the position of the cameras. This was used to determine the time window for the DIC and to evaluate if the pressure waves influenced the cameras.

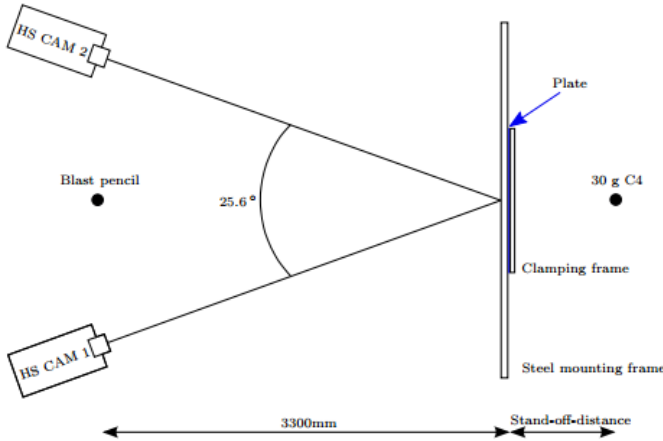


**Figure 6.3:** Camera set-up seen from above [22].

Table 6.1 give the order in which the experiments were performed. Three calibration tests were performed on a 15 mm thick steel plate at stand-off distance 250, 375 and 500 mm, to record the pressure along the plate profile. For the 0.8 mm thick component tests, three tests were performed at stand-off distance 250 mm and 375 mm, while six tests was performed at 125 mm due to problems with the DIC

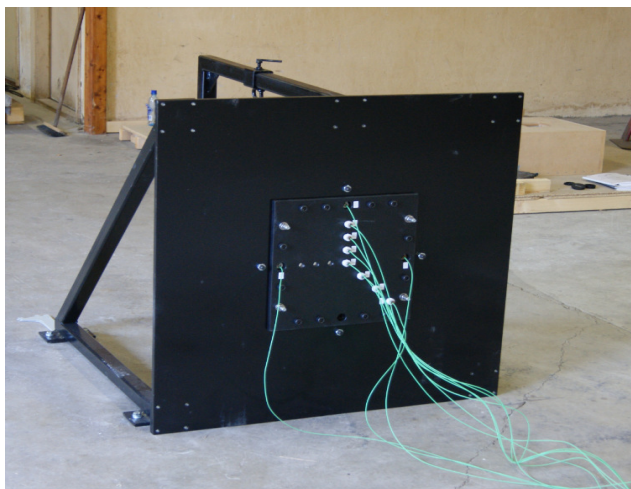
recordings. The estimated pressure given in Table 6.1 are estimated using ConWep.

**Table 6.1:** Performed experiments

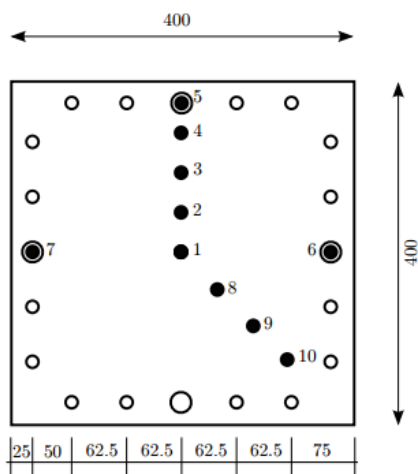
Plate thick- ness [mm]	Stand- off distance [mm]	Charge weight [g]	Estimated $P_{re}$ [bar]	1	2	3	4	5	6
15 Steel	250	30	114.2	R11	R12	R13	N/A	N/A	N/A
	375	30	37.50	R21	R22	R23	N/A	N/A	N/A
	500	30	15.82	R31	R32	R33	N/A	N/A	N/A
0.8 Steel	125	30	N/A	S11	S12	S13	S14	S15	S10
	250	30	N/A	S21	S22	S23	N/A	N/A	N/A
	375	30	N/A	S31	S32	S33	N/A	N/A	N/A

To validate the reflected pressure and sphericity of the pressure distribution for the target plates, calibration tests with pressure transducers mounted in the plate were performed. To reduce the risk of damaging the pressure sensors, validation tests at stand-off 125 mm was not performed. Seven pressure transducers were mounted in the plate along the normal and diagonal of the calibration plate, while three sensors (5,6 and 7) were mounted in the clamping frame. The sensors in the frame were present during both the calibration test and the component test, allowing to compare the pressure distribution and magnitude for the target plates with the rigid plates.

A break-wire was used to register the time from the detonation to the pressure arrives at the plate. Break-wire was only used for the calibration tests and for test S10. The recorded time of arrival was later used when the component test was to be evaluated. Test S10 was not recorded with DIC, however the time of arrival was recorded with break wire and the time of arrival is applied in the evaluation of plate S15. Figure 6.4a display the calibration rig and Figure 6.4b the location of the pressure transducers.



(a) Rigid plate mounted in front of frame



(b) Sensor numbering

**Figure 6.4:** Experimental set-up.

It is noted that the during the calibration, the rigid plate was mounted

on the opposite side of the frame, as seen in Figure 6.4a above. The pressure wave propagates 15 mm longer before striking the pressure sensors in the rigid plate, than the for the target plate. Thus, the time of arrival is expected to be slightly higher for the calibration than for the component tests. Another concern that should be noted is that turbulence may be generated along the plate edge since there is a 15 mm gap between the rigid mounting frame and the rigid plate, although this is probably vanishingly small.

As seen in 6.4b transducers 1-4 and 8-10 were located in the rigid plate, while 5,6 and 7 in the clamping frame. Transducer 1 was moved to the remaining position (lower part center) in the frame for the target plate experiments.

## 6.2 Experimental Results

### 6.2.1 Blast Loading

In order to describe and explain the dynamic plate response, the occurring pressure wave and the resulting dynamic loading were investigated. The reflected pressure was measured for three identical tests with the rigid steel plate at each stand-off, and compared with the measured pressure for the 0.8 mm Docol 600 DL target steel plates.

According to Spranghers [22], experiments have demonstrated that for free air blast loads, the pressure wave induces highly localized and fast material response which can be divided in to two different stadia; first, the shock impulse forces all material particles to move out-of-plane when they are initiated with initial velocities. Second,

when the shock wave has vanished, the additional plate deformation is only driven by the imparted momentum. This may be observed as elastic vibrations, which eventually comes to rest due to damping in the material and boundary.

The reflected pressure for the validation tests R12 and R23 are given in Figure 6.5 and the corresponding reflected pressure and arrival time is given in Table 6.2.

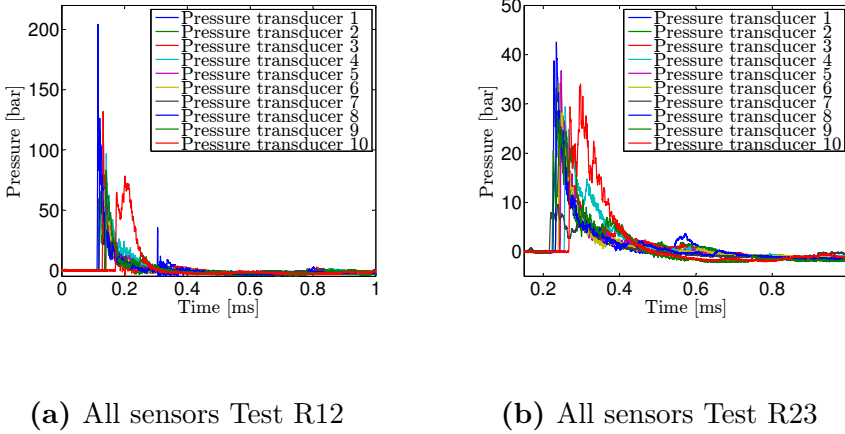


**Figure 6.5:** Reflected pressures calibration.

The pressure arrives at the center of the plate at 0.1124 ms for R12 and at 0.2261 ms for R23. It is observed that for R23 the pressure arrived at sensor 7 first which is located in the frame. This is probably due to the mentioned event of the sensors in the frame having 15 mm shorter stand-off distance.

The time of arrival varies due to the location of the pressure sensors and the distribution of pressure changes quickly with the time steps. The characteristic nature of a spherical airburst is observed as the pressure arrives at the center of the plate first and then is evenly distributed along the plate profile. The arrival time for the sensors in the frame is quite consistent. The effect of turbulence is also observed in the corner at sensor 10. The pressure in the corner arrives the latest, but the impulse is large due to prolonged positive phase.

The peak value of the reflected pressure wave drops from 204.3 bar at the center of the plate to only 45.2 bar for sensor 6 in the frame for test R12.

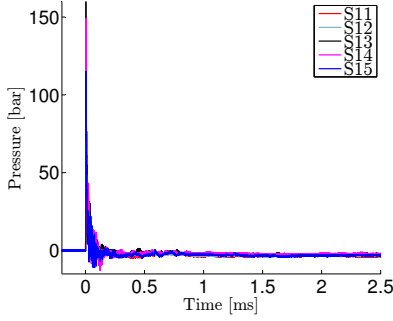
**Table 6.2:** Reflected peak pressures and corresponding time of arrival.

Sensor	$P_r$ R12	$t_a$	$P_r$ R23	$t_a$
1	204.3	0.1124	38.8	0.2261
2	65.6	0.1164	33.2	0.2324
3	131.9	0.1289	34.3	0.2431
4	96.8	0.1388	29.4	0.2554
5	53.3	0.1411	36.8	0.2447
6	45.2	0.1403	34.2	0.2397
7	68.8	0.1362	9.6	0.2173
8	126.3	0.1188	42.6	0.2324
9	83.1	0.1383	26.8	0.2240
10	78.1	0.1710	34.0	0.2677

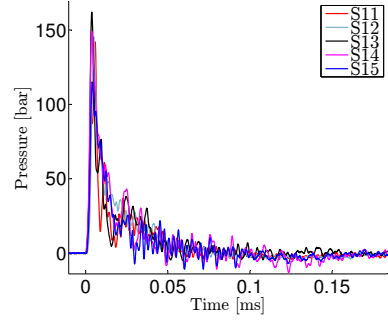
An example of a Matlab script for the plots from the calibrations test, are given in Appendix B.1 . The calculated impulse and time of arrival for each pressure sensor for test R12 and R23 are given in Appendix B.3. Time-pressure history plots are given for R11 and R12 in Appendix B.2 to display the compliance between the different pressure sensors.



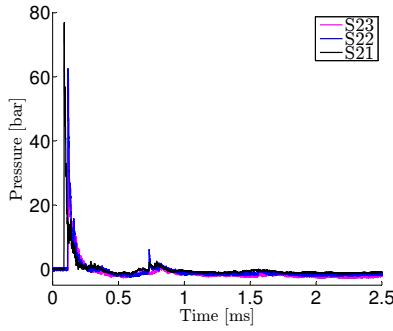
The repeatability for the target plate tests at each stand-off are displayed in Figure 6.6. The time-pressure history is quite consistent for each test at stand-off 250 mm and 375 mm, while for the closest stand-off the shift between the curves are slightly more distinct. However, the experiments display a good level of repeatability. The plots are given for sensor 1 (bottom sensor). Test S31 contained errors in the recordings for sensor 1 and are not presented.



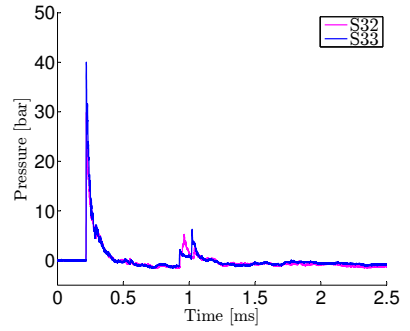
(a) Stand-off 125 mm



(b) Close-up stand-off 125 mm



(c) Stand-off 250 mm



(d) Stand-off 375 mm

**Figure 6.6:** Variations between the component tests for each stand-off distance.

Table 6.3 give the time of arrival, peak pressure, impulse of positive and negative phase and deflections for the component tests. The

## CHAPTER 6. EXPERIMENTS AT ØSTØYA

measured deflection is the deflection measured at the lab at NTNU after the plates were removed from the frame. The arrival time for test R23 are applied in both S31, S32 and S33 due to lack of break wire in test R22. The break wire did not go off for test R11, hence for tests S21, S22 and S23 arrival time from R12 is applied. The impulses and peak pressure are given for sensor 7. The arrival time is from sensor 7 for both R12 and R23.

**Table 6.3:** Results from component tests

	S11	S12	S13	S14	S15	S21	S22	S23	S31	S32	S33
Ta [ms] from calibration	0.0738*	0.0738*	0.078*	0.078*	0.078*	0.1362	0.1362	0.1362	0.2173	0.2173	0.2173
Peak Pressure [bar]	51.3	41.3	97.6	39.2	104.7	76.9	62.5	76.7	24.2	30.24	31.7
Positive Impulse [kPams]	115.4	95.8	132.6	148.7	133	139.2	121.0	146.6	104.0	108.7	122.3
Negative Impulse [kPams]	-185.1	-83.3	-98.5	-113.2	113.1	-31.0	-44.3	-81.0	-24.7	-24.5	-35.6
Max Z mid-point [mm] DIC	N/A**	N/A**	N/A**	N/A**	33.35	21.91	22.99	N/A**	15.84	17.68	16.95
Final Z mid-point [mm] DIC	N/A**	N/A**	N/A**	N/A**	28.43	16.60	17.26	N/A**	-7.69***	-7.22***	-6.84***
Measured Z from lab	30.0	29.2	28.8	30.3	28.0	16.5	18.3	18.3	8.1	7.9	9.1

\* No calibration test at stand-off 125 mm

\*\* No DIC, the trigger did not go off

\*\*\* Final deflection directed towards the impulse loading

The peak pressure, arrival time, positive and negative impulse for the sensors located in the frame are given for the calibration and the component test in table 6.4. Representative tests for each stand-off distance are chosen and time of arrival is chosen for sensor 7 for both

calibration tests.

**Table 6.4:** Comparison of calibration test and component test

Sensor	S22			R12			S33			R23		
	5	6	7	5	6	7	5	6	7	5	6	7
Arrival time from cal. [ms]		0.1362			0.1362			0.2173			0.2173	
Peak Pressure [bar]	75.4	67.6	52.9	53.3	45.2	68.8	31.8	32.9	31.7	36.8	34.2	9.6
Positive Impulse [kPa ms]	169.0	145.0	120.8	139.1	131.4	147.3	118.0	128.6	122.3	128.8	85.0	146.9
Negative Impulse [kPa ms]	91.4	-52.7	-44.3	-89.3	-82.4	-43.4	-34.6	-21.8	-35.6	-15.35	-15.35	-36.6

As mentioned, calibration test for stand-off 125 mm were not performed, but break wire were used for test S10 as done in the calibration tests. The arrival time for this test is used in the assessment of test S15. Table 6.5 give the results from stand-off 125 mm.

**Table 6.5:** Results from component test

Sensor	S15			
	5	6	7	
Arrival time [ms]		0.0738		
Peak Pressure [bar]	115.0	114.7	42.0	104.7
Positive Impulse [kPa ms]	116.1	148.4	120.9	133.0
Negative Impulse [kPa ms]	-148.0	-106.5	-131.6	-113.0

The correspondence between the peak pressure is sufficiently consistent for all stand-off distances, while the impulse are more divergent.

Test S15 have significantly higher peak pressure, but as the positive phase is very brief, the impulse corresponds with the impulse for the other stand-off distances. The positive and negative phases are difficult to define for several reasons; firstly, there is observed a second peak in the time-pressure history which interfere with either the positive or the negative phase. Secondly, for some tests the sensors tend to drift, the recorded pressure does not return to atmospheric pressure, it stabilizes at a negative value. This is a known problem for this type of pressure transducers with no obvious remedy, and thus ignored in this thesis. Nominally identical detonations are known to regularly produce different loads on structures from test to test due to a series of non- controlled factors as mentioned. The given impulse is therefore only a approximation.

Examples of negative and positive phase are given in Figure 6.7. It is noted that for some tests the second peak can not be avoided.

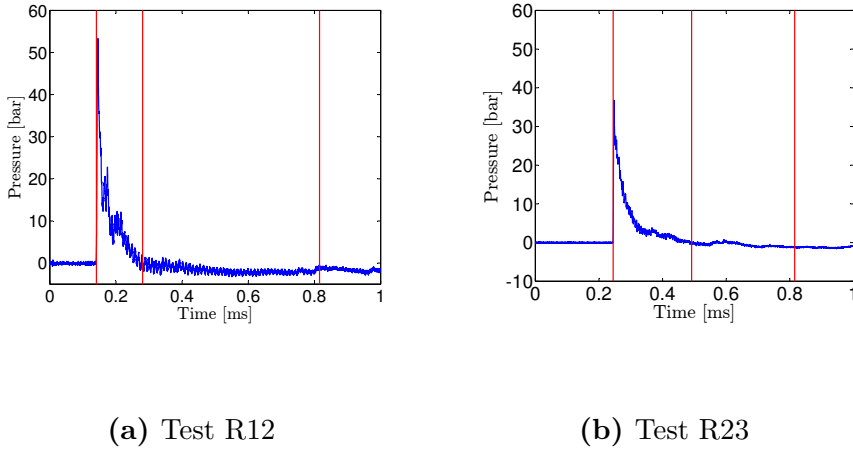


**Figure 6.7:** Limits for positive and negative phase for determining the impulse .

### 6.2.2 Plate response

Figure 6.8 displays the final deflection of plates from the different tests. The charge is positioned approximately at the center of the plate, resulting in an almost symmetric pressure distribution. Yield lines are specially observed in Figure 6.8a, which occurs when the detonation produces highly localized loading when the plate is located this close to the charge.

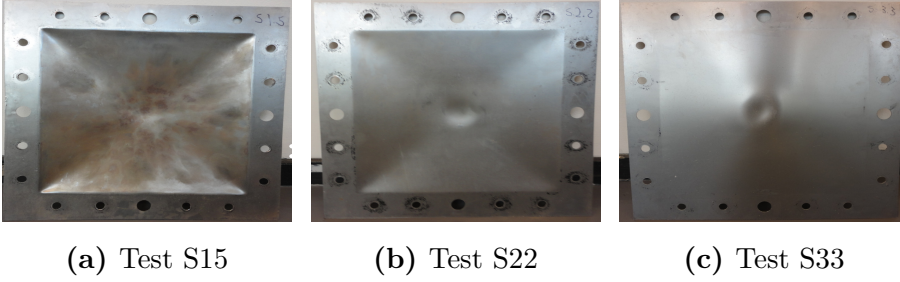


**Figure 6.8:** Deformed steel plates.

It is observed in Figure 6.8c that the permanent deflection of the plate is at the opposite side of the loading. This is due to the counter-intuitive reversed snap-buckling behaviour of the plate, which will be discussed in section 6.2.3.

The small eccentricity in the plate deformation may be caused by two factors; the charge may not be located at the exact center of the plate and the charge may not be completely spherical. Since the charge is this close to the plate, small differences in the location of the explosive may have large effects on the pressure profile along the plate. The charge was not casted in advance, thus not expected to be completely spherical. In some tests the DIC have some imperfections, these are expected to occur due to reflections in the steel plate from the daylight, but have not influenced the maximum and permanent deflection in this for the result presented.

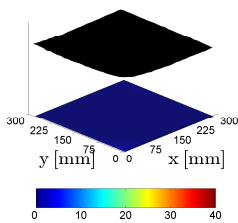
The deflection along the profile recorded with DIC tend to rapidly increase by 3-4 mm when the shock wave hits the blast pencil located in between the cameras. The deflections recorded after the shock wave has passed the cameras, are accordingly not reliable. This "jump" was at about 10 ms after the detonation. There is not observed any shift in the plate response after 4 ms for stand-off 125 mm and 250 mm, thus the deflections in Figure 6.9, 6.10 are only presented up to

4 ms for it to be easier to observe the time-pressure history and the corresponding time-displacement history during and just after the shock wave has passed.

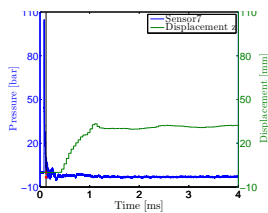
For the same reasons the pressure and deflection history are only given up to 8 [ms] for stand-off 375 mm to display the snap-buckling effect more in detail given in Figure 6.8c.

The displacement and the corresponding pressure for 6 points along time-displacement curve, including fringe plots of the plate at the different time steps are given for test S15, S22 and S33 in the figures below. These tests are representative for their adjacent stand-off distance.

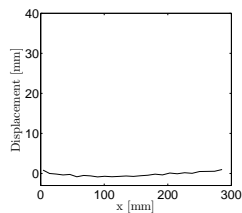




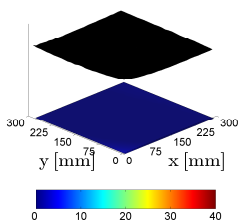
(a)  $t = 0.1218$  ms



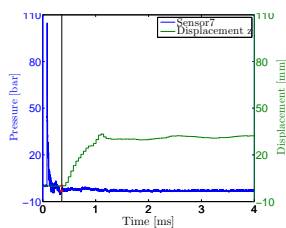
(b)  $t = 0.1218$  ms



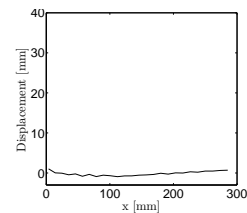
(c)  $t = 0.1218$  ms



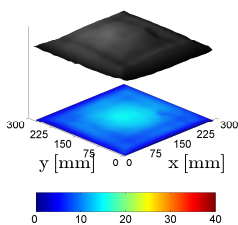
(d)  $t = 0.3599$  ms



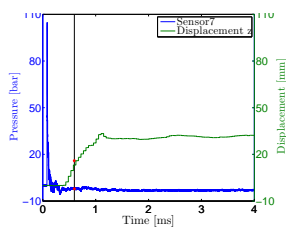
(e)  $t = 0.3599$  ms



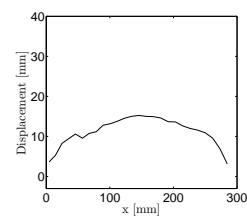
(f)  $t = 0.3599$  ms



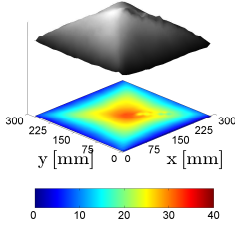
(g)  $t = 0.5980$  ms



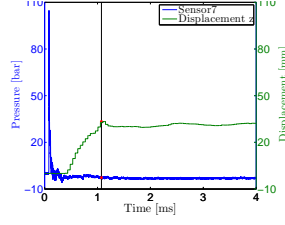
(h)  $t = 0.5980$  ms



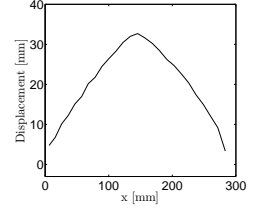
(i)  $t = 0.5980$  ms



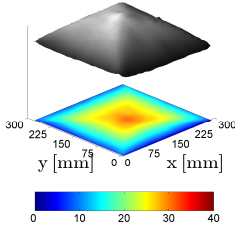
(j)  $t = 1.0742$  ms



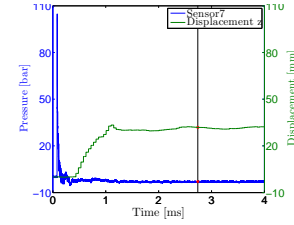
(k)  $t = 1.0742$  ms



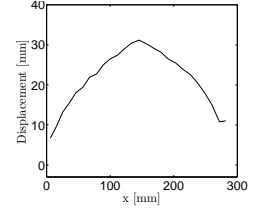
(l)  $t = 1.0742$  ms



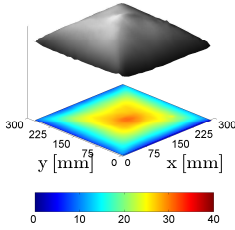
(m)  $t = 2.741$  ms



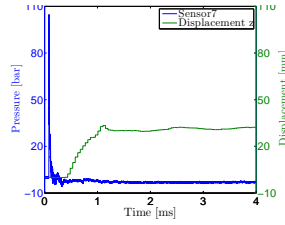
(n)  $t = 2.741$  ms



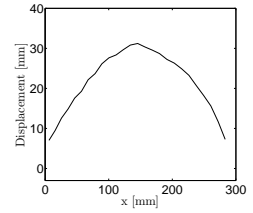
(o)  $t = 2.741$  ms



(p)  $t = 4.884$  ms

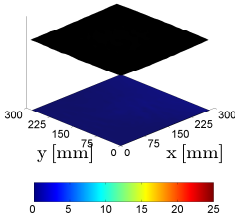


(q)  $t = 4.884$  ms

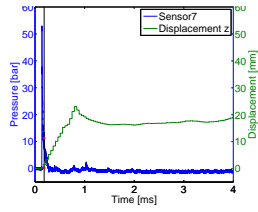


(r)  $t = 4.884$  ms

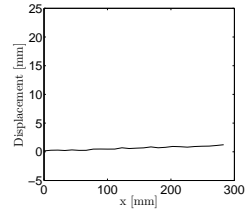
**Figure 6.9:** Displacement field and contour map from DIC for test S15



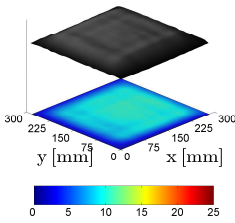
(a)  $t = 0.1839$  ms



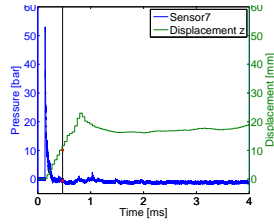
(b)  $t = 0.1839$  ms



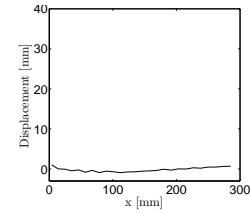
(c)  $t = 0.1839$  ms



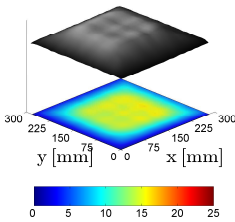
(d)  $t = 0.4696$  ms



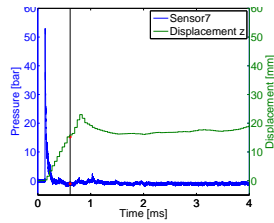
(e)  $t = 0.4696$  ms



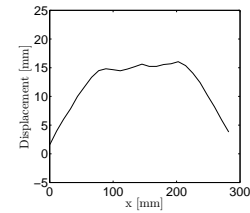
(f)  $t = 0.4696$  ms



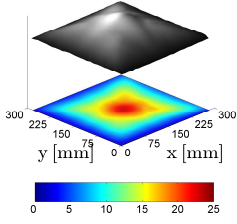
(g)  $t = 0.6125$  ms



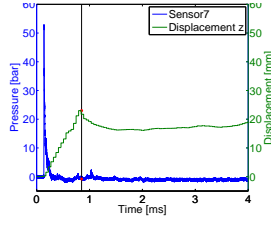
(h)  $t = 0.6125$  ms



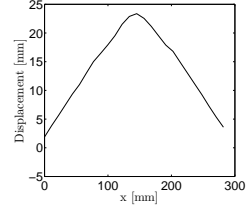
(i)  $t = 0.6125$  ms



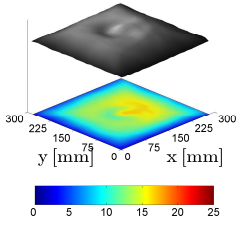
(j)  $t = 0.8506$  ms



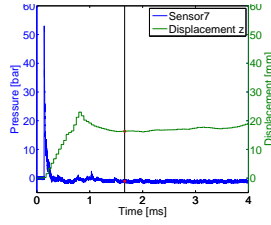
(k)  $t = 0.8506$  ms



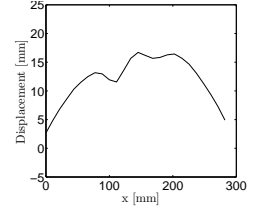
(l)  $t = 0.8506$  ms



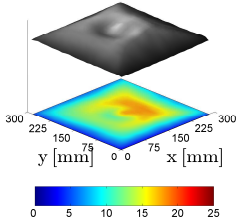
(m)  $t = 1.660$  ms



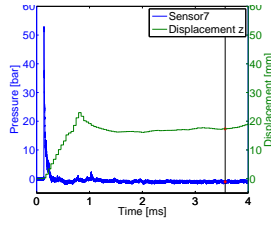
(n)  $t = 1.660$  ms



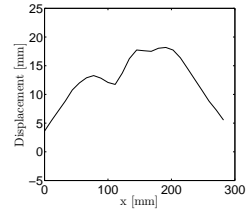
(o)  $t = 1.660$  ms



(p)  $t = 3.565$  ms

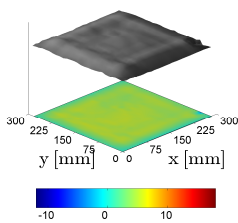


(q)  $t = 3.565$  ms

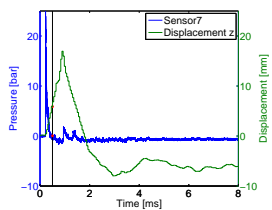


(r)  $t = 3.565$  ms

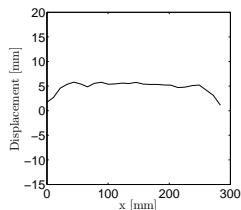
**Figure 6.10:** Displacement field and contour map from DIC for test S22



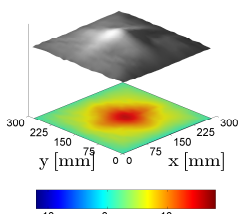
(a)  $t = 0.5034$  ms



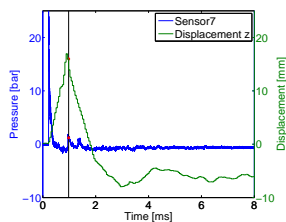
(b)  $t = 0.5034$  ms



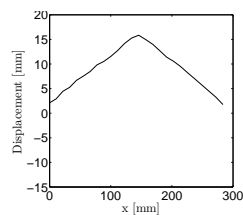
(c)  $t = 0.5034$  ms



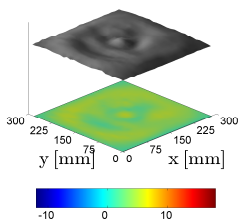
(d)  $t = 0.9796$  ms



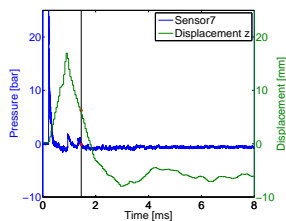
(e)  $t = 0.9796$  ms



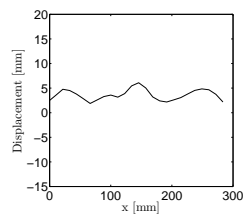
(f)  $t = 0.9796$  ms



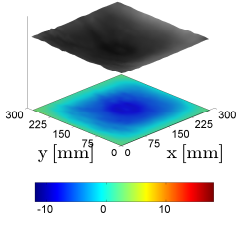
(g)  $t = 1.4558$  ms



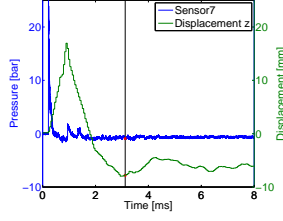
(h)  $t = 1.4558$  ms



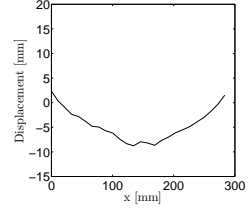
(i)  $t = 1.4558$  ms



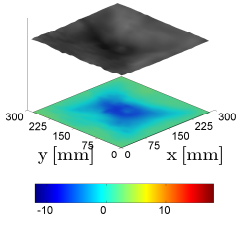
(j)  $t = 3.1225$  ms



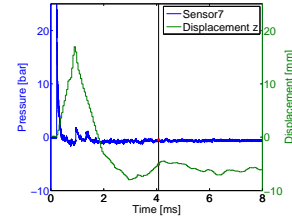
(k)  $t = 3.1225$  ms



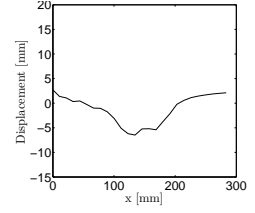
(l)  $t = 3.1225$  ms



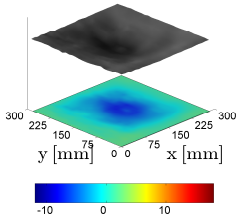
(m)  $t = 4.0748$  ms



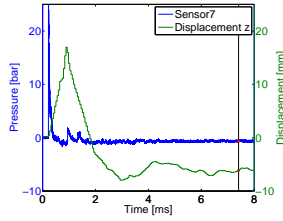
(n)  $t = 4.0748$  ms



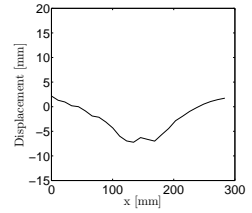
(o)  $t = 4.0748$  ms



(p)  $t = 7.4082$  ms



(q)  $t = 7.4082$  ms



(r)  $t = 7.408$  ms

**Figure 6.11:** Displacement field and contour map from DIC for test S33

### 6.2.3 Counter-intuitive reversed snap-buckling

For the detonations performed at stand-off distance 375 mm, the plate is observed to deform in the loading direction, before it "snaps back" towards the load direction and elastically vibrate about a negative equilibrium. The permanent deflection is negative loading direction as presented in Section 6.2.2. This phenomenon is known as counter-intuitive snap-buckling behaviour or reversed snap-buckling and was initially reported by Symmonds and Yu [52]. For flat plates, the reverse snap-buckling only take place with elastic-plastic deformation, but for a cylindrical or spherical panel it may occur for visco-elastic, elastic and elastic-plastic [53].

Previous experiments display that when the counter-intuitive phenomenon appear, the deformations depend strongly on the loading and the initial conditions. As investigated in [53], the behaviour are typically provoked by the loading being applied in a certain range, initiating the structure with a certain initial velocity. After deflecting in the direction of the loading, the structure snaps through to the opposite side. For some cases the deflection remains at that side (with negative deflections), while in others it snaps back in the loading direction and remains on the positive side. This is also the preliminary conclusion in [54]. After a large amount of numerical simulations performed with aluminium, the velocity range in which counter-intuitive behaviour is more likely to occur is predicted. Conditions that have been experienced to influence the velocity range are the dimensions of the specimen, material properties, boundary conditions and loading shape.

The studies presented so far indicate that this behaviour is unpredictable. The initial imperfections and environmental conditions seem to influence the final deformation dramatically. What may have been proven is that larger initial velocity is needed for simply supported boundary conditions, that is; increased boundary restrain

makes the rebounding easier to occur. [54]

A parametric study is performed in Chapter 7 regarding the counter-intuitive snap-buckling behaviour of the plate. The stand-off distance is varied about 375 mm to further provoke counter-intuitive snap buckling behaviour.



# Chapter 7

## Numerical simulations

In this chapter a parametric study is carried out to investigate how different parameters influence the plate response. The results from this section are further discussed in Chapter 8.

It is noted that there is a natural randomness in the kinematic molecular technique implemented in Impetus-Afea, thus small adjustments that may not influence the solution in commercial FEM, may be prominent in the following numerical simulations.

During the experiment none of the plates failed, thus fracture is thus not simulated.

### 7.1 Parameter study

The following variables are investigated in parameter study:

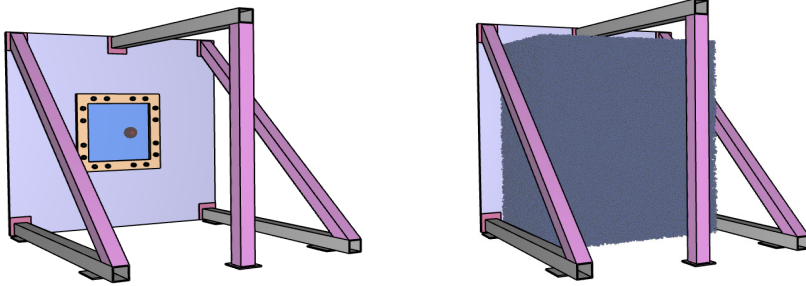
- Boundary Conditions

- Total number of particles
- Charge weight
- Stand-off variations
- Plate thickness

In addition, the material models calibrated in Chapter 4 are compared for large strains to display any differences in the plate response. The counter-intuitive snap-buckling is further provoked for different stand-off distances and charge weight.

### Procedure

The entire rig from the experiments is modelled in Impetus-Afea to get as identical conditions in the numerical simulations, as in the experiments as possible. The geometry in the numerical model is given in Figure 7.1.



(a) Experimental rig with HE-particles      (b) Experimental rig with air particles

**Figure 7.1:** Experimental set-up in Impetus-Afea with air particles.

In the numerical simulations 941,735 particles were used to model the air and 58,265 particles were used to model the high explosives, in

total 1,000,000 particles. The finite element mesh for the rig consists of 3754 elements with 15x15x0.8 mm 64-noded hexahedron giving a total of 179,264 nodes, with one element over the plate thickness. The charge geometry is spherical and the the volume of the charge is decided by the amount of C4. The simulations is terminated after 3 ms due to computational costs. The run time for each simulation is not given, as it is approximately between 4 and 5 hours for all simulations, except for parametric study of the snap-buckling behaviour and the study of number of particles. The parametric study is mainly preformed for stand-off distance 125 mm, except for the simulations with the counter-intuitive snap-bukling behaviour.

The pre-stressing of the bolts is run in a separate simulation, before the constraints in the clamped frame are implemented in the main simulation. The steel-steel coefficient of friction is set to 0.3 in the clamping connection. Keyword example from Impetus-Afea for stand-off distance 125 mm, are given for the pre-tensioning and the blast simulation in Appendix D.1 and Appendix D.2, respectively.

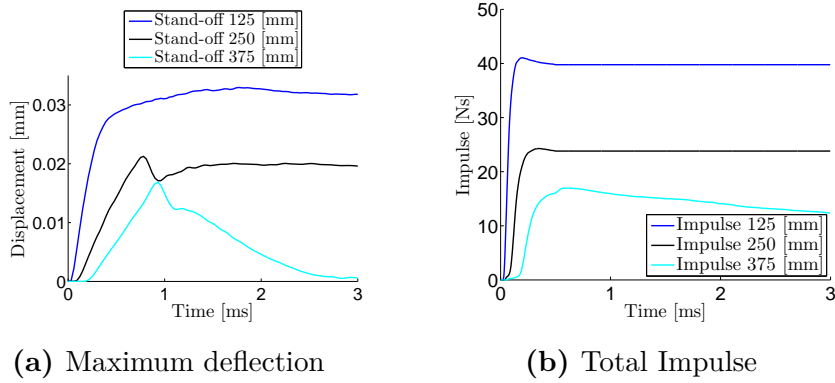
### 7.1.1 Results from the different stand-off distances

A simulation is performed for each stand-off distance at Østøya. The time-deflection history for the different stand-off distances and the corresponding total impulse accumulated to the plate, are given in Figure 7.2.

The simulation for stand-off 375 mm have been run for 6 ms, due to the counter-intuitive snap buckling behaviour that occurs at the respective stand-off distance and the total permanent deflection is given for 6 ms. Table 7.1 compare the maximum permanent deflection from Impetus-Afea with the deflection recorded with DIC.

**Table 7.1:** Deflection for the different stand-off distances

Stand-off [mm]	$Z_{perm}$ [mm]	Impetus-Afea	Measured $Z_{perm}$ [mm]	% Deviation
125		31.85	28.43	10.74
250		19.60	17.26	11.94
375		-6.03	-7.22	16.10


**Figure 7.2:** Plate response and applied impulse for the different stand-off distances.

The corresponding accumulated impulse coincide well with the deflection history. The impulse is calculated by integrating the particle-structure contact forces from both air and HE- particles in time. The negative trend after the peak values observed, is due to the air pressure on the opposite side of the plate being larger than the pressure on the front of the plate. Hence, the air particles may give a positive and negative contribution to the total impulse, while the HE-particles can only impart a positive impulse. [55]

The pressure is an average over the whole exposed area, and when the plate deforms, the exposed area changes. The impulse is therefore given in Ns.

### 7.1.2 Boundary conditions

A penalty based contact formulation is used for clamping of the frame in Impetus. During the experiments the M12-8.8 bolts were pre-stressed with a torque of 200 Nm. Employing a clamping force of this magnitude, would probably have caused the bolts to yield. However, it was not observed any plastic deformation in the bolts during the experiments. It is therefore likely that the bolts are more rigid than what is given as a nominal value in the material certificate.

Due to great uncertainties in the calculation of the achieved clamping force in the bolts, it is assumed that each bolt is pre-stressed to 534 MPa. This is a prevalent clamping stress for M12-8.8 bolts [56].

This is not the correct clamping force according to the experiments performed at Østøya, but it is applied in the following numerical simulations in this parametric study.

To examine the effect of the underestimated clamping of the frame, an analysis with a likely stress of 1300 MPa from the pre-tensioning is run. The yield and fracture strain in the bolts are also increased in this simulation to prevent plasticity in the bolts.

To investigate if the clamping of the frame have great influence on the plate response, fixed and simply supported boundary conditions are also simulated. For the simply supported simulation the coefficient of friction and the clamping force in the bolts are set to zero.

The effect of the clamped frame are given in Figure 7.3 and in Ta-

ble 7.2, where the permanent deflection from the different boundary conditions are compared to the restraining used in the later simulations, i.e 534 MPa.

**Table 7.2:** Permanent displacement for boundary conditions

	Simply supported	Prestressed 534 [MPa]	Prestressed 1300 [MPa]	Fixed
Permanent $\Delta Z$ [mm]	32.35	31.85	31.25	30.52
% deviation	1.6	-	1.9	4.2

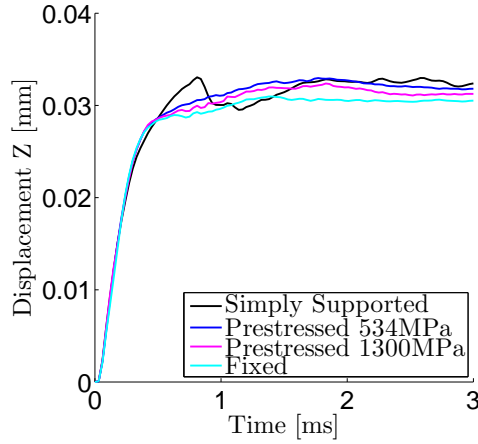


**Figure 7.3:** Displacement for the different restraining conditions applied.

It is observed that the clamping of the frame give a maximum error of the permanent deflection of 4.2 %. Visual inspection of the plates after the test showed that there was slippage at the boundaries, see

Figure 7.4. The diameter of the bolt holes with most slippage was measured to be 14.7 mm at the most, which is an increase of 1.7 mm. Hence, the restraining can be not be assumed to be completely fixed.



**Figure 7.4:** Bolt holes at the boundary

Due to the underestimated stress in the clamping connection, it is expected that the deflection in this parametric study are overestimated with between 1.9 and 4.2 %.

### 7.1.3 Number of particles

Impetus-Afea apply both high explosives (HE) and air particles when simulating blast loading. To establish the correct gas dynamics during an explosion, the air particles and high explosives need to be given about the same particle mass. The C4 and the air particles are assigned initial velocities in random directions. The number of high explosive particles are about 5.83 % of the total number of particles in the analysis. The *total* number of particles on the other hand may be adjusted.

A study of total number of particles of 500,000 and 2,000,000 are performed and compared to the chosen number of particles of 1,000,000,

which is applied in the simulations.

The distribution of HE particles along the plate for the first time steps of the simulation are given in Figure 7.5 below.

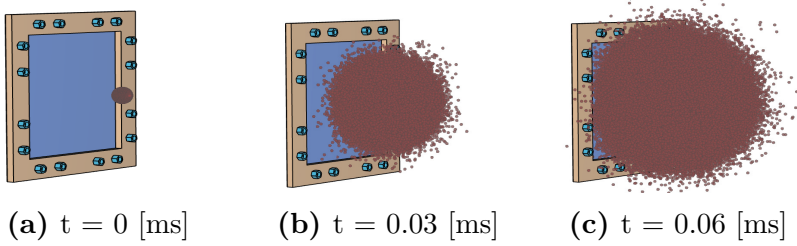


**Figure 7.5:** HE-particles distribution along the target plate.

The total number of particles and corresponding number of air and HE-particles are given in Table 7.3.

**Table 7.3:** Number of air and HE particles

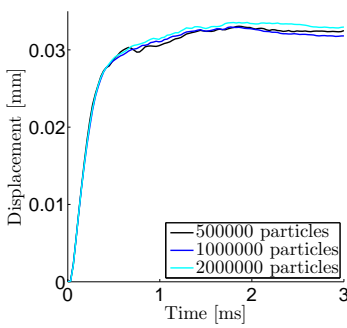
Total number of particles	Air particles	HE particles
500000	470 868	29 132
1000000	941 735	58 265
2000000	1 883 471	116 529

The number of particles, permanent deflection and computational time for each analysis is given in the Table 7.4. The time-deflection history is given in Figure 7.6a and the impulse for the different amount of particles are given in Figure 7.7b.

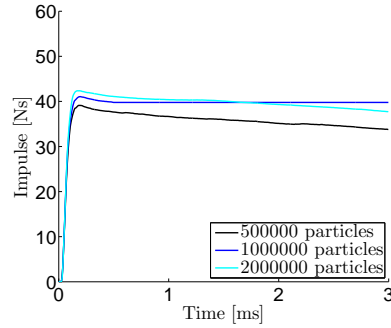


**Table 7.4:** Deflection and computational time

Number of particles	$Z_{perm}$ [mm]	CPU time [h:min:s]
500000	32.46	05:09:00
1000000	31.85	08:05:34
2000000	32.95	14:55:09



(a) Maximum displacement



(b) Total Impulse

**Figure 7.6:** Plate response and total impulse applied for the different amount of particles.

As the number of particles is increased, the curve becomes smoother with less oscillations. The energy level is independent of the number of particles, but as the energy is divided between several particles, a finer load distribution along the plate is obtained. Fewer particles give more energy to each particle, which may give an uneven distribution of particles along the plate. It is though noted, that a small amount of particles does not necessarily predict an underestimated deflection, as it is in this case.

For all practical purposes, the solution is assumed has converged. The difference in deflection is negligible if the number of particles is to be further increased.

### 7.1.4 Charge weight

The influence of the charge weight is investigated and the time-deflection curve is given in Figure 7.7a. By varying the charge weight with 16.7 % give approximately 11-16 % difference in permanent deflection as given in Table 7.5.

**Table 7.5:** Permanent deflection for different charge weights.

	25 [g]	30 [g]	35 [g]
Permanent $\Delta Z$ [mm]	26.80	31.85	35.40
% deviation	15.86	-	11.15

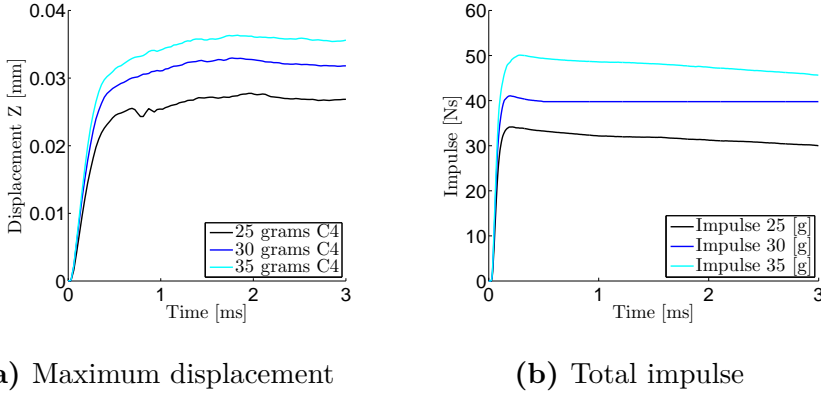


**Figure 7.7:** Plate response and total impulse applied for the different charge weights.

Variations in charge weight give a cubic volume increase, resulting in significant increase in number of high explosive particles.

### 7.1.5 Material model

All simulations are run with the material model calibrated from the extensometer values. As discussed in Chapter 4, the material behaviour for large deformations is reliant upon material parameters displaying correct post-necking behaviour. To display possible differences between the two material models for large plastic deformations, an analysis with charge weight of 55 g is run.

The maximum plastic strain occurs at the boundaries as seen in Fig-

ure 7.9 and are of 65 % and 60 % for the material model from the extensometer and the material model based on DIC values, respectively. Table 7.6 display the permanent deflection. Even though the permanent deflection is practically equal, the plastic straining along the plate profile is noticeable different, see Figure 7.9.

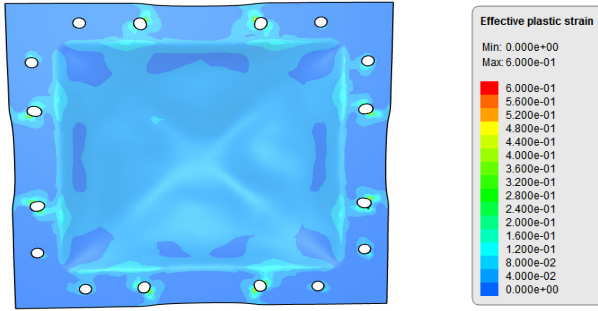


**Figure 7.8:** Plastic strain fringe plot from Impetus-Afea Extensometer values

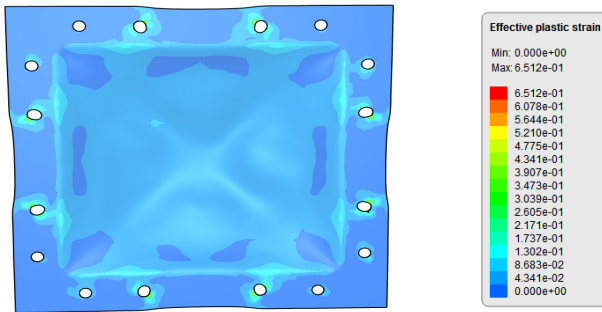
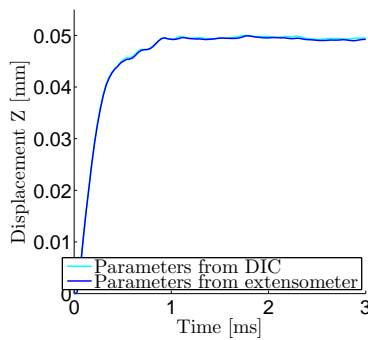


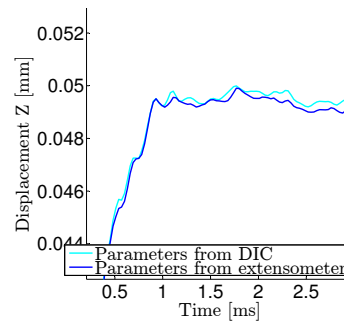
**Figure 7.9:** Plastic strain fringe plot from Impetus-Afea DIC values.

**Table 7.6:** Permanent deflection for the different material models.

	Extensometer material param- eters	DIC material parameters
Permanent $\Delta Z$ [mm]	49.25	42.50



(a) Maximum deflection



(b) Close-up on plate response

**Figure 7.10:** Plate response and total impulse applied for the different material models.

### 7.1.6 Stand-off variations

The stand-off distance between the explosive charge and the plate is varied by  $\pm 15$  mm to display how the stand-off influence the reflected pressure. Figure 7.7 give the permanent deflection for the different stand-off distances.

**Table 7.7:** Permanent deflection for the different stand-off distances

	110 [mm]	125 [mm]	140 [mm]
Permanent $\Delta Z$ [mm]	26.90	31.85	35.62
% deviation	15.55	-	10.17

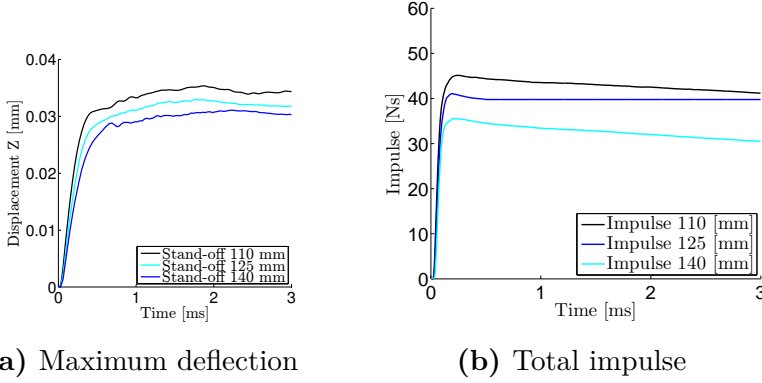


**Figure 7.11:** Plate response and applied impulse for different stand-off distances

The total impulse applied to the plate varies with stand-off distance, as the intensity of the front is inverse proportional to the square of the distance. As the charge is moved closer to the sample surface, the fraction of particles that impact the plate increase, and the total impulse transmitted to the the plate rises.

For instances involving airblast or air overpressure, the relation for the scaled Hopkinson-Cranz distance  $Z$  is

$$Z = \frac{R}{W^{1/3}} \quad (7.1)$$

where  $R$  is the range from the detonation and  $W$  is the charge weight expressed equivalent TNT mass. From this, it is observed that a adjustment in distance gives a cubic decrease of the loading.

### 7.1.7 Plate thickness

The thickness of the target plates used at Østøya were measured to control the actual thickness. The actual thickness was at the most 0.015 mm over the given thickness of 0.8 mm. To display the difference in deflection due to different plate thickness, simulations with plate thickness of 0.78 mm and 0.82 mm is run. To capture what small differences in plate thickness, yet large percentage difference yields for the plate response, simulations are performed for 0.70 mm and 0.90 mm as well. Figure 7.12 give the deflection of the plate for the different plate thickness’.

**Table 7.8:** Results

	0.70 [mm]	0.78 [mm]	0.80 [mm]	0.82 [mm]	0.90 [mm]
Permanent $\Delta Z$	34.82	31.81	31.85	32.79	28.02
% deviation	9.3	0.1	-	3.0	12.0

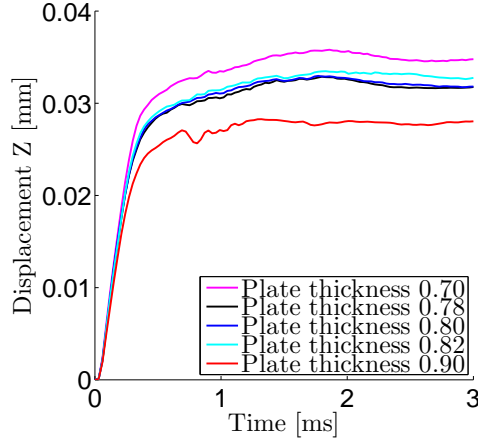


**Figure 7.12:** Variations of plate thickness.

By changing the thickness with  $\pm 2.5\%$  the deflection changes with  $0.1\%$  and  $3\%$  for thickness  $0.78\text{ mm}$  and  $0.82\text{ mm}$  respectively. It may be observed from the curve that deflection is larger for  $0.82\text{ mm}$  than for  $0.80\text{ mm}$ , and that  $0.80\text{ mm}$  and  $0.78\text{ mm}$  are almost equal throughout the time-deflection history. This is highly non-physical as the plates bending rigidity being a cube of the thickness as given in Eq. (7.2).

$$D = \frac{Et^3}{12(1 - \nu^2)} \quad (7.2)$$

Table 7.9 below give bending stiffness for the different plate thickness' studied, the deviation from the bending stiffness for the  $0.8\text{ mm}$  steel plate and the percentage deviation of the permanent deflection from the  $0.8\text{ mm}$  steel plate..



**Table 7.9:** Comparison of deflection and rigidity of the plates

	0.7 [mm]	0.78 [mm]	0.8 [mm]	0.82 [mm]	0.9 [mm]
Plate stiffness D [Nmm]	8.575	11.864	12.8	13.784	18.225
Deviation of D %	33.0	7.3	-	7.7	42.4
Deviation of $\Delta Z$ %	9.3	0.1	-	3.0	12.0

By changing the plate stiffness, it is expected to get noticeable differences in the maximum deflection of the plates, although that is not what observed. This may be an example of the natural diversity in Impetus-Afea, but this is only a vast assumption.

## 7.1.8 Counter-intuitive buckling

During the experiments, the rather rare phenomenon counter-intuitive reversed snap-buckling occurred at stand-off 375 mm. As described in chapter 6.2.3, the initial velocity seem to influence this behaviour in particular. To investigate the effect of the different initial velocities of the plate, the stand-off distances and charge weight are varied.

It is suspected that a reduction in applied loading, hence less plastification of the plate, will provoke further snap-buckling behaviour. Simulations are performed for stand-off distances of 405 mm and 417 mm, and setting the charge weight to 21 g. It was chosen to terminate the simulations after 6 ms due to computational costs. The permanent deflections are not completely stabilized after 6 ms, but sufficient enough to observe the snap-buckling behaviour and the peak deflections.

The maximum peak deflection and the permanent deflection are given in Table 7.10 and the time-displacement curves are given in Fig-

ure 7.13. It is noted that the permanent deflection is towards the loading.

**Table 7.10:** Max and permanent deflection for the snap-buckling behaviour

Stand-off distance [mm]	Max peak deflection	Permanent deflection $\Delta Z$
375	13.42	-6.03
375 with 21 [g]	13.15	-8.17
405	13.59	-8.56
417	14.86	-8.49

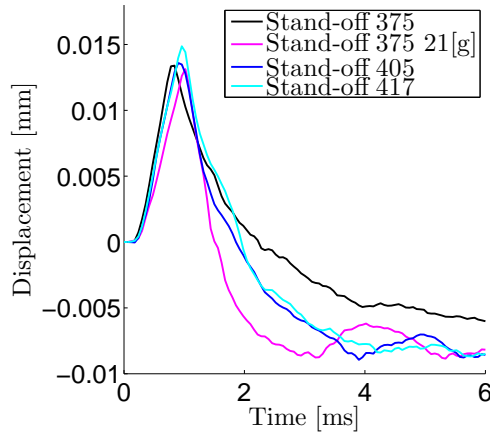


**Figure 7.13**

It is observed that the reducing the loading, hence the initial velocity of the plate, resulted in increased negative deflections of the plate.

# Chapter 8

## Discussion

The primary goal with this thesis was to qualitatively display the numerical results compared to the experiments at Østøya and investigate which parameters that greatly influence the response of the plate.

This chapter will compare and discuss the accuracy of the results and possible sources of error.

### 8.1 Experiment compared to numerical simulations

The maximum permanent deflection from Abaqus/Explicit, Impetus-Afea and the DIC measurements, are given for the different stand-off distances in Figure 8.1 and in Table 8.1. The mean test is given if available. It is noted that the values from Abaqus/Explicit is obtained with SimLab Metal Model and do not coincide completely with the deflection history obtained in the mesh sensitivity study.

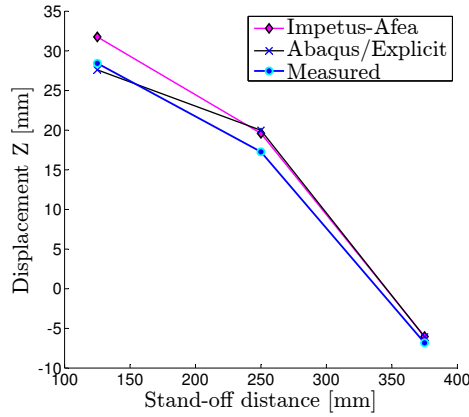


**Figure 8.1:** Permanent deflections for Impetus-Afea, Abaqus/Explicit and the experimental results.

**Table 8.1:** Comparison of permanent deflection

Stand-off distance [mm]	Impetus-Afea $Z_{perm}[mm]$	Abaqus/Explicit $Z_{perm}$ [mm]	Experiment $Z_{perm}[mm]$
125	31.85	27.6	28.43
250	19.60	17.97	17.26
375	-6.03	-6.08	-7.22

A comparison of the corresponding reflected pressure obtained from ConWep, Abaqus/Explicit's blast-load function (based on ConWep) and calibration tests during the experiments are given in Table 8.2. The pressure is given for the center node of the plate and at the plate boundary (sensor 7). The ratio between the pressure at center and at the boundary is also given.

**Table 8.2:** Comparison of pressure distribution along plate

Standoff distance [mm]	Pressure [MPa]		
	ConWep	Abaqus Explicit	Calibration test
125 <sub>center</sub>	55.44	32.3	N/A*
125 <sub>edge</sub>	20.06	9.12	10.46**
Ratio	0.36	0.28	-
250 <sub>center</sub>	11.42	8.78	20.44
250 <sub>edge</sub>	6.82	5.34	6.88
Ratio	0.60	0.61	0.34
375 <sub>center</sub>	3.75	3.53	3.78
375 <sub>edge</sub>	2.67	2.60	3.42***
Ratio	0.71	0.74	0.90
500 <sub>center</sub>	1.58	1.54	2.03
500 <sub>edge</sub>	1.26	1.27	1.54
Ratio	0.80	0.83	0.76

\* No calibration test at closest stand-off distance

\*\* From component test S15 sensor 7

\*\*\* Sensor 6 (left side) applied due to errors in the pressure readings for sensor 7

As observed in the table above, the ratio between the peak pressure at the center of the plate and the pressure at the edge, coincide better for the different approaches when the stand-off distance is increased. Abaqus/ Explicit interprets its own ConWep based load-function, hence the slightly different pressure distributions. When the charge is located this close to the plate, the pressure wave propagating to the sensors located in the frame (i.e sensor 6 and 7), is partly side-on pressure. The angle between the surface normal and the direction of the propagating wave passing the pressure sensors in the frame, is too large for the pressure recorded by these sensors to be purely head-on pressure. In [22], a relation for the reflected pressure due to

a certain angle of incidence  $\theta$ , is determined

$$P(t) = P_I(1 + \cos\theta - 2\cos^2\theta) + P_R\cos^2\theta \quad (8.1)$$

where  $P(t) = P_I$  when  $\cos\theta = 0$  and  $P(t) = P_R$  when  $\cos\theta = 1$  [22].

When the stand-off distance increase, the pressure will hit the frame mainly as head-on pressure and the ratio between the the pressure at the center and at the boundary will increase.

For stand off distance 125 mm the pressure difference between the center and the frame is substantial, but since the experimental results are limited at this stand-off, there is no base for further comparison. For the remaining stand-off distances, it is observed that Abaqus/ Explicit give consequently lower peak pressure estimations than ConWep, and these are again lower than the pressure recorded in the experiments. A comparison of the impulse between Abaqus/-Explicit and the calibration tests are given in Table 8.3.

**Table 8.3:** Comparison of impulse from Abaqus/Explicit and calibration test

Stand-off distance [mm]	Impulse Abaqus/Ex- plicit [kPams]	Impulse Calibra- tion test [kPams]
250 <sub>center</sub>	263	301
250 <sub>edge</sub>	197	147
375 <sub>center</sub>	166	146
375 <sub>edge</sub>	145	85
500 <sub>center</sub>	177	143
500 <sub>edge</sub>	153	101

It may seem like Abaqus/Explicit under-predict the peak pressures,

while the impulse is overestimated when the stand-off distance is increased. If this is the case, Abaqus/explicit underestimate the deflection for close range blasts while, the impulse is overestimated for increasing stand-off distances. This assumption coincide well with the permanent deflections displayed in Table 8.1, and that ConWep is more accurate for larger stand-off distances.

Identical detonations produce different loads imparted to the plate from test to test due to a series of non-controllable factors that affect the pressure profile, and hence the plate response. Special attention are paid to sources of errors that causes a different distribution and intensity in the propagating pressure wave. As given in Table 7.5 and Table 7.7 the charge weight and the stand-off distance have proven in the previous parametric study to have great impact when it comes to the plate response.

Different charge geometries give different spread in particles. Lower spread of particles give a larger impulse and thus larger deformations. This has been investigated in [57] where it was demonstrated that the geometry of the charge, constitute considerable influence on the particle distribution and total impulse. The charges utilized at Østøya was not casted in advance, hence probably not perfect spherical and the pressure distribution not symmetric for all component tests. During the experiments it was observed asymmetric deflections along the plate, which indicate that either the charge geometry or the alignment of the charge was not perfectly symmetrical.

Impetus-Afea fails to display the peak deflection that occurs just after the pressure wave has vanished. However, when the loading is reduced by reducing the charge weight or the plate properties is increased, the peak becomes visible. Typical example of this is displayed in Figure 7.7a for the charge weight and Figure 7.12 displaying the peak for the 0.9 mm thick plate. It may be observed that the peak deflection does not occur when the displacement pass approximately

30 mm, and it is implied that further plastification of the material prevents the elastic peak. This peak is displayed in the DIC measures from Østøya and are given in the time-displacement history in Figure 6.9 and from Abaqus/Explicit in Section 5.2.2, although the deflections are also a few percentage lower than in Impetus-Afea. This may imply that the impulse in Impetus-Afea is just substantial enough for the plate to adequately plastify and skip this elastic peak deflection. It was not performed any experiments with increasing load, thus this behaviour can not be confirmed in the plate response from experiments.

The counter-intuitive reversed snap buckling behaviour was discovered in Impetus-Afea as well, and the percentage deviation from the measured permanent deflection was 16.5 %. This is a greater deviation than for the other stand-off distances. As previously mentioned, small variations in certain parameters results in great differences in the initial velocity, which provoke the snap-buckling behaviour to certain extents. The restraining along the boundaries have been experience in [54] to also have great impact on the counter-intuitive behaviour. The snap-buckling behaviour are easier to provoke when the boundaries are further constrained [54]. Due to the clamping force applied in the numerical model not being completely recreated compared to the experiments, it may be implied, that the permanent deflection in Impetus-Afea is lower as the boundary is less constrained.

To investigate if any fluid-structure-interaction effects occurs, a comparison between the pressure distribution from the component test and the calibration test is performed for the sensor in the frame (sensor 5 and 7) in Figure 8.2.



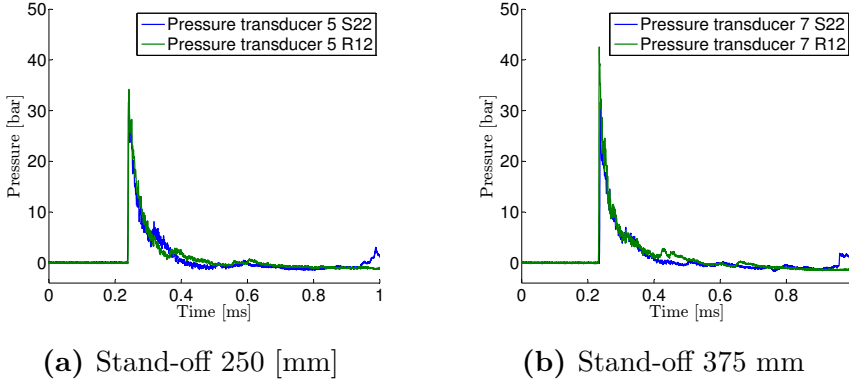


**Figure 8.2:** Comparison of pressure distribution from calibration and component test.

It is not observed any FSI effect in the pressure curves, as the pressure distribution for the calibration test and the component test is practically equal. The pressure propagation is not delayed due to the deformed plate. As seen in Figure 6.9, the plate does not respond until after the shock wave has vanished. This is typical for an impulse loading, where the plate response is driven by the imparted momentum.

Five tests were performed at stand-off distance 125 mm, but as mentioned in Chapter 6, but only test S15 is recorded with DIC. The deflection of the midpoint was still measured with a caliper for all five tests, and the measured deflection is in general larger for the first four tests.

When performing experiments, a natural variation in the results is expected and hence the mean value is normally presented. In this

thesis the results from test S15 is presented as it is the only test available, even though it is not necessarily a representative test for the adjacent stand-off. The difference in the measured permanent deflection for tests at stand-off distance 125 mm, is only about 1-2 mm. However, this give a percentage difference in the permanent deflection from what is suspected to be the mean value.

Appendix B.2 display the time-pressure curves for calibration test R11 and R12. A second peak is observed in the time-pressure history which, is too close to the initial shock front to be a reflection from any surfaces. This peak is also observed in the component tests given in Figure 6.6. Similar behaviour are displayed in [58], where it is observed that the incident shock wave is followed by a second shock wave whose amplitude is smaller. This is explained in [59]; when the charge is ignite, an incident shock wave propagates from the contact surface (the surface between the surroundings and the initial gaseous mixture) towards the centre of the charge. When this rarefaction wave sufficiently decreases the pressure from the burnt gas with respect to the ambient pressure, a shock wave is created that propagates towards the centre of the charge. When this shock wave reaches the centre of the charge, it is reflected (implosion) and then propagates in the same direction as the initial incident shock wave. The secondary shock is rarely mentioned in the literature, and whether the same conditions were applied in the mentioned experiments are not fully looked into. The secondary shock occurs for both spherical and hemispherical charges. The phenomenon may be an explanation of the second peak observed, however this should be further investigated.

Primarily the charge weight and stand-off distance seem to influence the time-deflection history substantially and by only changing any of these variables with a few percent yields great difference in the plate response.

The numerical simulations in Impetus-Afea are experienced to reproduce the experimental permanent and peak midpoint deflections with a high level of accuracy.

### 8.1.1 Abaqus/Explicit vs Impetus-Afea

In the preliminary study, Impetus-Afea displayed completely different permanent deflections than Abaqus/Explicit, when employing the same simplified model. Abaqus/Explicit gave a good approximation, while the permanent deflection in Impetus-Afea was highly underestimated as displayed in Figure 5.6. Based on the results obtained in this simplified study, it seem to be more crucial for Impetus-Afea to have more accurate loading conditions and geometry, to display accurate behaviour than for traditional FEM software (i.e. Abaqus/Explicit).

The are difference between the describing of the load in Abaqus/Explicit and Impetus-Afea. The discrete particle based method have a natural randomness in the describing of the load, and small differences in e.g how the particles are packed in the charge, may give different results. The mentioned uniquely higher order elements in Impetus-Afea describe the plastic behaviour more exact than in Abaqus/Explicit.

The same element size of the plate are employed in both numerical codes, but as Impetus-Afea has a demand of convergence for the number of particles as well to describe the distribution of the particles (loading) better. The main difference between the two numerical codes except from the element formulations, are how the load is applied. Impetus-Afea transfers energy through rapidly expanding air and HE particles, which is simply based on pure physical force transfer between the rigid particles and the plate. While the Lagrangian

approach in Abaqus/Explicit apply the load, which is based on empirical formulas, as an symmetrically distributed load.

There are two main disadvantages with using ALE approach compared to the discrete particle approach; the mapping step between the Eulerian and the Lagrangian mesh may cause an advection error and the Eulerian-Lagrangian approach is also very computational expensive.

### 8.1.2 Sources of error in the numerical model

As emphasized earlier, the boundary conditions in the numerical simulations are not exact, but according to the results presented in Section 7.1.2, the restraining of the clamped frame did not influence the result in particular. The maximum deviation is 4 %, and this is when the boundary is assumed to be fixed. However, it is observed slippage at the boundaries. Hence, the clamping connection in the frame is not completely fixed. It may be concluded that error due to inaccurate boundary conditions, is less than 4.2 %.

In [44] the fracture strain is 0.81 for the respective material. It is noted that during the experiments a charge of 55 [g] would probably shear failure at the boundaries, but this it not considered in this thesis. An increase in loading is only to demonstrate the effect of having material parameters calibrated to fracture if that is what simulated. The material calibrated, display a softer behaviour as displayed in Chapter 4, but this difference seem to be vanishingly small according to the comparison of permanent deflections given in Table 7.6.

The plate response measured during the experiments at Østøya is over-predicted by about 10 % compared to the numerical model in Impetus-Afea. This gives a conservative estimate for all stand-off distances within the experimental limitations of this thesis. Overall,

the consistency between the experiment and the numerical simulation using Impetus-Afea is sufficient and of great acceptance. Small adjustment in the numerical simulations, will probably increase the accuracy even further.

### 8.1.3 Results compared to other experiments and numerical simulations

A limited comparison with previously performed experimental and numerical simulations are given in this section. Studies regarding the discrete particle approach is emphasized in the particular.

In [60], the influence of stand-off distance is investigated for fully clamped steel plates. It is concluded that for stand-off distances less than the plate radius (in this case 13-40 mm), the blast load is considered to be localized, ideally to the center of the plate. For stand-offs distances greater than the plate radius (i.e 100 - 300 mm), the loading is uniformly distributed over the entire plate.

This is similar to observations made during the experiments performed at Østøya at 125 mm. Perfect yield lines are observed in the plate profile due to highly localized pressure. In the numerical simulations the localization is particularly observed for stand-off 110 mm, and to some extent for stand-off 125 mm and 140 mm.

The accuracy of the particle based approach have been examined in [61]. Extruded aluminium panels were subjected to localized impulse loading by the impact of explosively accelerated saturated sand at several stand-off distances. The overall conclusion was that the numerical model described the problem with good accuracy taking the complexity of the problem into account.

The results from the discrete particle approach are very close to the result from Ls-Dyna using fully coupled Lagrangian-Eulerian approach. It is found that both codes over predict the measured permanent deflection by about 15 % in [13].

As mentioned in the Chapter 2, the results obtained in [26], have also displayed numerically robustness and computational efficiency, compared to traditional ALE simulations.

In previous work, the discrete particle method has been proven to display both the applied loading and the plate response. However, the discrete particle method implemented in non-linear numerical codes is still not quantitatively covered in the literature.

# Chapter 9

## Concluding Remarks

The dynamic response of Docol 600 DL steel plates subjected to free air blast loading has been numerically studied employing the discrete particle based approach implemented in Impetus-Afea. The results from the numerical simulations have been validated against experimental results performed at Østøya.

- ConWep is proven to be a fast and powerful tool in estimating the reflected pressure when compared to the experiments performed in this thesis. The coincidence between the experiments and ConWep is improving when the stand-off distance is increased as expected.
- A pure Lagrangian formulation using the simplified blast-load description based on ConWep, has been performed in Abaqus/Explicit. Based on the results obtained in this thesis, it is indicated that Abaqus/Explicit underestimate the peak pressures for all stand-off distances, while overestimating the impulse for stand-off distances over 250 mm.
- To get more reliable results from the experiments, several mea-

tures should have been conducted to exclude the avoidable errors that may have been introduced. This includes the charge weight being accurately weighed and casted in advance, the alignment of the charge should have been more accurately measured. In addition, an approach for more sufficient measurements of the plate deflection in-situ and a picture of the final deflection of the plate taken with DIC, to ensure that the measured permanent plate deflection obtained is adequate.

- A parametric study is performed to display the influence different parameters have on the plate response. Small adjustments during the experiment in e.g. stand-off distance or charge weight have great influence on the peak and permanent deflections. It may be implied that the numerical simulations may not be the greatest source of error in this study.
- The experiments display a good level of repeatability. The peak pressure and impulse from the experiments are presented with a sufficient level of accuracy for each stand-off.
- A simplified problem was applied in both Abaqus/Explicit and Impetus-Afea, where Impetus highly underestimates the permanent deflection. It is implied that in Impetus-Afea, it is more crucial to model the geometry and loading conditions more exact, than for commercial FEM (i.e. in this case Abaqus/Explicit).
- The plate response is suspected to primarily rely on the load description. As stated in earlier work, the main challenge is describing the load accurately. The particle based approach interpreted in Impetus-Afea have proven with a high level of accuracy to reveal the dynamic plate response when different loading and plate properties are applied.



# Chapter 10

## Further work

- By increasing the loading during the experiments by either increasing the load weight or decrease the stand-off distance, fracture in the target plate could have been investigated. Comparison with numerical simulations. By comparing the two different material models applied in this thesis, it would be expected to observe more evident differences for the larger strains.
- Performing material testing and more thorough calibration using LS-OPT or similar code to get a more accurate material model.
- Performing ALE simulations and studying the effect of FSI for the performed study. Compare the accuracy between the two different approaches and possible sources of errors. Which technique describes the loading best.
- Further investigation of the counter-intuitive reversed snap buckling. Varying parameters under the experiment and display if Impetus-Afea picks up, display the same behaviour with varying the different parameters. Does Impetus-Afea over-or underestimate the appearance of this phenomenon.

- Performing simulations in several numerical codes, e.g. Ls-Dyna, to compare if the blast-load functions employed give similar results to what obtained in Abaqus/Explicit.
- Further investigation of the second peak pressure observed in several pressure plots.

# Bibliography

- [1] Review of methods for calculating pressure profiles of explosive air blast and its sample application. <http://scholar.lib.vt.edu/theses/available/etd-043099-163540/unrestricted/AJMKCTHESIS.PDF>. Retrieved 02.05.2014.
- [2] Kristoffer H Andersen and Fredrik Børsum Hernandez. Numerical simulations of docol 600 dl steel plates subject to blast loading master thesis. Master Thesis.
- [3] KH Safari, J Zamani, SMR Khalili, and S Jalili. Experimental, theoretical, and numerical studies on the response of square plates subjected to blast loading. *The Journal of Strain Analysis for Engineering Design*, 2011.
- [4] GN Nurick and JB Martin. Deformation of thin plates subjected to impulsive loading a review: Part i: theoretical considerations. *International Journal of Impact Engineering*, 1989.
- [5] Norman Jones, Tevfik Osman Uran, and Sedat Ahmet Tekin. The dynamic plastic behavior of fully clamped rectangular plates. *International Journal of Solids and Structures*, 1970.
- [6] SB Menkes and HJ Opat. Broken beams. *Experimental Mechanics*, 1973.

- [7] Lawrence E Malvern. *Introduction to the Mechanics of a Continuous Medium*. Number Monograph. 1969.
- [8] Jean Donea, Antonio Huerta, J-Ph Ponthot, and Antonio Rodríguez-Ferran. Arbitrary lagrangian–eulerian methods. *Encyclopedia of computational mechanics*, 2004.
- [9] Simulia abaqus 6.12 user manual. [http://www.tu-chemnitz.de/projekt/abq\\_hilfe/docs/v6.12](http://www.tu-chemnitz.de/projekt/abq_hilfe/docs/v6.12), 2013.
- [10] Lstc. ls-dyna keyword user’s manual, version 971. livermore software technology coporation. January 2007.
- [11] Autodyn. <http://www.ansys.com/products/autodyn.asp>.
- [12] Joint research center (jrc). europlexus user’s manual. commissariat a l’energie atomique (cea).
- [13] T Børvik, AG Hanssen, M Langseth, and L Olovsson. Response of structures to planar blast loads—a finite element engineering approach. *Computers & Structures*, 2009.
- [14] U.s. army corps of engineering, naval facilities engineering command (preparing activity) and air force civil engineering support agency. unified facilities criteria (ufc) structures to resist the effect.
- [15] SJ Pi, DS Cheng, HL Cheng, WC Li, and CW Hung. Fluid–structure-interaction for a steel plate subjected to non-contact explosion. *Theoretical and Applied Fracture Mechanics*, 2012.
- [16] Stephen D Boyd. Acceleration of a plate subject to explosive blast loading-trial results. Technical report, DTIC Document, 2000.
- [17] MD Olson, GN Nurick, and JR Fagnan. Deformation and rupture of blast loaded square plates predictions and experiments. *International Journal of Impact Engineering*, 1993.

## BIBLIOGRAPHY

---

- [18] RL Veldman, J Ari-Gur, and C Clum. Response of pre-pressurized reinforced plates under blast loading. *International Journal of Impact Engineering*, 2008.
- [19] GS Langdon and GK Schleyer. Inelastic deformation and failure of profiled stainless steel blast wall panels. part i: experimental investigations. *International Journal of Impact Engineering*, 2005.
- [20] GS Langdon and GK Schleyer. Inelastic deformation and failure of profiled stainless steel blast wall panels. part ii: Analytical modelling considerations. *International Journal of Impact Engineering*, 2005.
- [21] JZ Ashani and AK Ghamsari. Theoretical and experimental analysis of plastic response of isotropic circular plates subjected to underwater explosion loading. *Materialwissenschaft und Werkstofftechnik*, 2008.
- [22] K Spranghers, I Vasilakos, D Lecompte, H Sol, and J Vantomme. Full-field deformation measurements of aluminum plates under free air blast loading. *Experimental mechanics*, 2012.
- [23] K Spranghers, I Vasilakos, D Lecompte, H Sol, and J Vantomme. Numerical simulation and experimental validation of the dynamic response of aluminum plates under free air explosions. *International Journal of Impact Engineering*, 2013.
- [24] K Spranghers, I Vasilakos, D Lecompte, H Sol, and J Vantomme. Identification of the plastic behavior of aluminum plates under free air explosions using inverse methods and full-field measurements. *International Journal of Solids and Structures*, 2014.
- [25] Lars Olovsson and IMPETUS Afea. Corpuscular method for airbag deployment simulations. 2007.

- [26] L Olovsson, AG Hanssen, T Børvik, and M Langseth. A particle-based approach to close-range blast loading. *European Journal of Mechanics-A/Solids*, 2010.
- [27] T Børvik, L Olovsson, AG Hanssen, KP Dharmasena, Håkan Hansson, and HNG Wadley. A discrete particle approach to simulate the combined effect of blast and sand impact loading of steel plates. *Journal of the Mechanics and Physics of Solids*, 2011.
- [28] Wikipedia. Wikipedia deflagration definition. <http://en.wikipedia.org/wiki/Deflagration>. Retrieved 20.04.2014.
- [29] Wikipedia. Explosions definition. <http://en.wikipedia.org/wiki/Explosion>. Retrieved 31.01.2014.
- [30] Philip S Bulson. *Explosive loading of engineering structures*. CRC Press, 2002.
- [31] Gaz Specialization website. Definiton of blast waves. <http://www.cngspw.com/vbooks/ShowSubject.asp?SubjectID=8222>. Retrieved 06.06.2014.
- [32] Wilfred Edmund Baker. *Explosions in air*. University of Texas Press Austin, 1973.
- [33] Glasstone blogspot. Mach stem. [http://glasstone.blogspot.no/2013\\_10\\_01\\_archive.html](http://glasstone.blogspot.no/2013_10_01_archive.html). Retrieved 22.02.2014.
- [34] Sam Mannan. *Lees' Loss prevention in the process industries: Hazard identification, assessment and control*. Butterworth-Heinemann, 2004.
- [35] WJ Macquorn Rankine. On the thermodynamic theory of waves of finite longitudinal disturbance. *Philosophical transactions of the Royal Society of London*, 1870.

## BIBLIOGRAPHY

---

- [36] KG Rakvåg, NJ Underwood, GK Schleyer, T Børvik, and OS Hopperstad. Transient pressure loading of clamped metallic plates with pre-formed holes. PhD Thesis.
- [37] Wikiepedia lagrangian mesh transformation. [http://en.wikiversity.org/wiki/Nonlinear\\_finite\\_elements/Lagrangian\\_and\\_Eulerian\\_descriptions](http://en.wikiversity.org/wiki/Nonlinear_finite_elements/Lagrangian_and_Eulerian_descriptions), Retrieved 31.05.2014.
- [38] Ted Belytschko, Wing Kam Liu, Brian Moran, and Khalil Elkhodary. *Nonlinear finite elements for continua and structures*. John Wiley & Sons, 2013.
- [39] Hans-Joachim Bungartz and Michael Schäfer. *Fluid-structure interaction: modelling, simulation, optimisation*. Springer, 2006.
- [40] Mathisen K.M. Tkt4197 lecture 7: Solution of the dynamic equilibrium equations by explicit direct integration. *Lecture notes in TKT4197*, 2013.
- [41] David J Benson. Explicit finite element methods for large deformation problems in solid mechanics. *Encyclopedia of Computational Mechanics*.
- [42] T Børvik, OS Hopperstad, T Berstad, and M Langseth. A computational model of viscoplasticity and ductile damage for impact and penetration. *European Journal of Mechanics-A/Solids*, 2001.
- [43] Plesha Michael E Cook Robert D, Malkus David S and Witt Robert J. *Concepts and applications of finite element method*. John Wiley & Sons. Inc., 2002.
- [44] Gaute Gruben, Egil Fagerholt, Odd Sture Hopperstad, and Tore Børvik. Fracture characteristics of a cold-rolled dual-phase steel. *European Journal of Mechanics-A/Solids*, 2011.

- [45] Egil Fagerholt. Field measurements in mechanical testing using close-range photogrammetry and digital image analysis. PhD Thesis.
- [46] Bing Pan, Dafang Wu, and Liping Yu. Optimization of a three-dimensional digital image correlation system for deformation measurements in extreme environments. *Applied optics*, 2012.
- [47] MA Sutton, JH Yan, V Tiwari, HW Schreier, and JJ Orteu. The effect of out-of-plane motion on 2d and 3d digital image correlation measurements. *Optics and Lasers in Engineering*, 2008.
- [48] Bulmash G Kingery CN. Air blast parameters from tnt spherical air burst and hemispherical surface burst. 1984.
- [49] Jens Kristian Holmen. Private communication.
- [50] Hopperstad O.S Borvik T. Tkt4135 lecture: The tension test. *Lecture notes in TKT4135*, 2013.
- [51] L Vistenes H Olovsson and Hansen A G. Introduction course to the impetus afea solver. 2013.
- [52] PS Symonds and TX Yu. Counterintuitive behavior in a problem of elastic-plastic beam dynamics. *Journal of Applied Mechanics*, 1985.
- [53] Sh U Galiev. Distinctive features of counter-intuitive behavior of plates and shells after removal of impulse load. *International journal of impact engineering*, 1997.
- [54] QM Li, LM Zhao, and GT Yang. Experimental results on the counter-intuitive behaviour of thin clamped beams subjected to projectile impact. *International journal of impact engineering*, 1991.
- [55] Olovsson lars mail correspondance, retrieved 03.06.2014.



- [56] Torque bolts. Retrieved 25.04.2014.
- [57] E A Melby and H S Eide. Blast loaded aluminium plates: Experiments and numerical simulations master thesis. Master Thesis.
- [58] PE Sauvan, I Sochet, and Sophie Trelat. Analysis of reflected blast wave pressure profiles in a confined room. *Shock Waves*, 2012.
- [59] B Vanderstraeten, M Lefebvre, and Jan Berghmans. A simple blast wave model for bursting spheres based on numerical simulation. *Journal of Hazardous materials*, 46(2):145–157, 1996.
- [60] N Jacob, GN Nurick, and GS Langdon. The effect of stand-off distance on the failure of fully clamped circular mild steel plates subjected to blast loads. *Engineering Structures*, 2007.
- [61] Haydn NG Wadley, Tore Børvik, Lars Olovsson, John J Wetzel, Kumar P Dharmasena, Odd Sture Hopperstad, VS Deshpande, and John W Hutchinson. Deformation and fracture of impulsively loaded sandwich panels. *Journal of the Mechanics and Physics of Solids*, 2013.



# Appendix A

## Kingery-Bulmash Chart (Ch. 3.5)

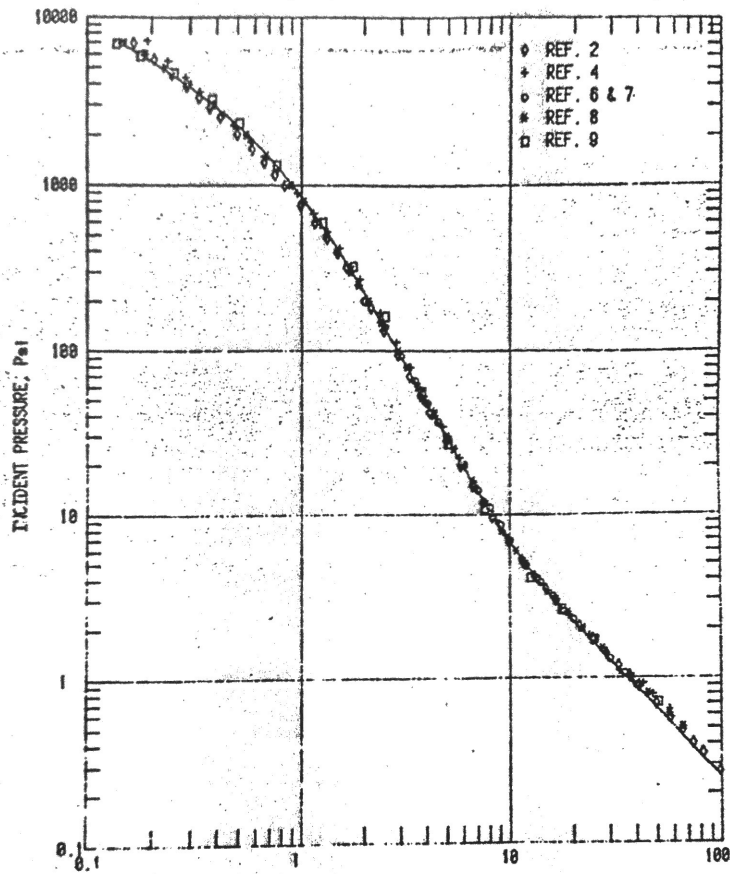


Figure A.1: Scaled distance Kingery-Bulmash

# Appendix B

## Experimental Results (Ch. 6)

## B.1 Matlab Script

```

1
2 %Calibration test R23
3
4 % Importing data from specific test
5
6 testdata=importdata('R22.csv');
7
8 t=testdata.data(:,1);
9 p=testdata.data(:,2:11);
10 bw=testdata.data(:,12);
11
12 p1 = testdata.data(:,2);
13 % Converting time from s to ms
14
15 t=t*10^3;
16
17 % Pressure transducer specific values
18
19 maxp=[180 70 140 100 60 50 70 130 90 80]; ...
        % Value above max pressure at the specific pressure ...
        transducers
20 t1pick=[3.990 1.974 2.485 3.65 3.000 2.8489 4.155 ...
        3.2949 3.2945 2.991]*10^-1; % ...
        Approximate time at the end of positive impulse
21 t2pick=[7.968 7.8032 8.0934 8.4746 8.1509 8.4076 ...
        8.0845 7.975 8.580 6.247]*10^-1; % ...
        Approximate time at the end of negative impulse
22
23 % Correcting curves according to time of detonation
24
25 top=p1(1);
26 count=1;
27
28 while top<=2
29     count=count+1;
30     top=p1(count);
31 end
32
33 figure(11);
34 plot(t,p1,'linewidth',1.6);

```

```

35 hold on;
36 grid on;
37
38 tp1=t(count);
39 p1line=[tp1 tp1];
40 line=[-1000 1000];
41 plot(p1line,line,'r','linewidth',1.6);
42 axis([0 20 -1 6]);
43 xlabel('Time [ms]','fontsize',24);
44 ylabel('Response','fontsize',24);
45 set(gca,'fontsize',24);
46
47 t=t(count:end);
48 t=t-t(1);
49 p=p(count:end,:);
50
51 ta=zeros(1,10);
52 t1=zeros(1,10);
53 t2=zeros(1,10);
54 impulse_pos=zeros(1,10);
55 impulse_neg=zeros(1,10);
56
57 for i=1:10
58     %Find time of arrival
59     top=p(1,i);
60     count=1;
61
62     while top≤3
63         count=count+1;
64         top=p(count,i);
65     end
66
67     ta(i)=t(count);
68     tacount=count;
69
70     % Define time of positive impulse t1 and negative ...
71     impulse t2
72     count=1;
73
74     while t(count)≤t1pick(i)
75         count=count+1;

```



```

75     end
76
77     t1count=count;
78     t1(i)=t(t1count);
79
80     while t(count)≤t2pick(i)
81         count=count+1;
82     end
83
84     t2count=count;
85     t2(i)=t(t2count);
86
87     tpos=t(tacount:t1count);
88
89     ppos=p(tacount:t1count,i);
90
91     tneg=t(t1count:t2count);
92     pneg=p(t1count:t2count,i);
93
94     impulse_pos(i)=trapz(tpos,ppos);    % Given in bar ...
95     impulse_neg(i)=trapz(tneg,pneg);    % Given in bar ...
96
97     times ms
98     time ms
99
100
101     taline=[ta(i) ta(i)];
102     t1line=[t1(i) t1(i)];
103     t2line=[t2(i) t2(i)];
104
105     figure(i);
106     plot(t,p(:,i),'linewidth',1.6);
107     hold on;
108     grid on;
109     plot(taline,line,'r','linewidth',1.6);
110     plot(t1line,line,'r','linewidth',1.6);
111     plot(t2line,line,'r','linewidth',1.6);
112     axis([0 10.0 -10 maxp(i)]);
113     xlabel('Time [ms]','fontsize',24);
114     ylabel('Pressure [bar]','fontsize',24);
115     set(gca,'fontsize',24);
116 end
117
118

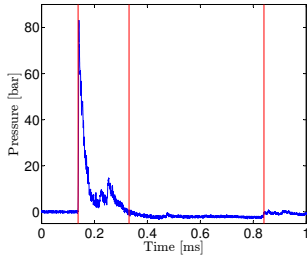
```

```

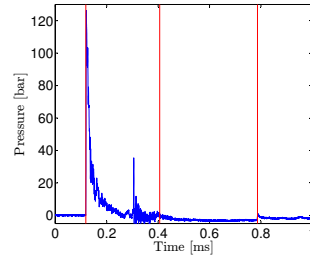
114 ta = [0.2261 0.2324 0.2431 0.2554 0.2447 0.2397 0.2173 ...
        0.2324 0.2240 0.2677];
115
116
117 figure(12);
118 plot(t,p(:,1),t,p(:,2),t,p(:,3),t,p(:,4),'linewidth',1.6);
119 axis([0 10 -5 140]);
120 xlabel('Time [ms]','fontsize',24);
121 ylabel('Pressure [bar]','fontsize',24);
122 set(gca,'fontsize',24);
123 legend('Pressure transducer 1','Pressure transducer ...
        2','Pressure transducer 3','Pressure transducer 4');
124
125 figure(13);
126 plot(t,p(:,1),t,p(:,8),t,p(:,9),t,p(:,10),'linewidth',1.6);
127 axis([0 10 -5 100]);
128 xlabel('Time [ms]','fontsize',24);
129 ylabel('Pressure [bar]','fontsize',24);
130 set(gca,'fontsize',24);
131 legend('Pressure transducer 1','Pressure transducer ...
        8','Pressure transducer 9','Pressure transducer 10');
132
133 figure(14);
134 plot(t,p(:,1),t,p(:,5),t,p(:,6),t,p(:,7),'linewidth',1.6);
135 axis([0 10 -5 100]);
136 xlabel('Time [ms]','fontsize',24);
137 ylabel('Pressure [bar]','fontsize',24);
138 set(gca,'fontsize',24);
139 legend('Pressure transducer 1','Pressure transducer ...
        5','Pressure transducer 6','Pressure transducer 7');

```

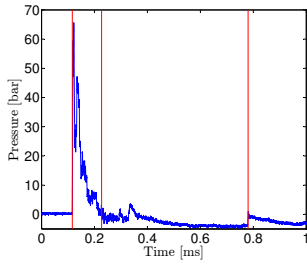
## B.2 Pressure Curves from Calibration Tests



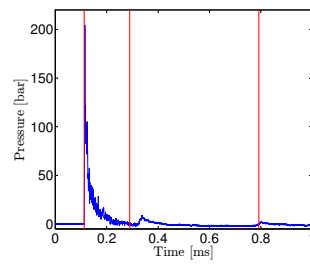
(a)



(b)

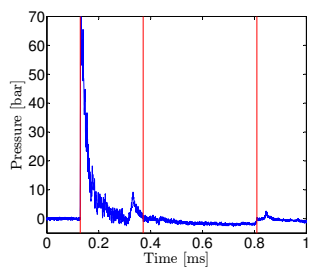


(c)

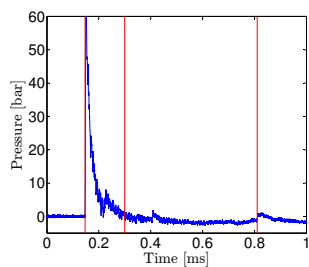


(d)

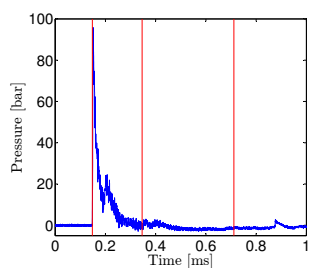
**Figure B.1:** Calibration R12 Pressure curves displaying second peak



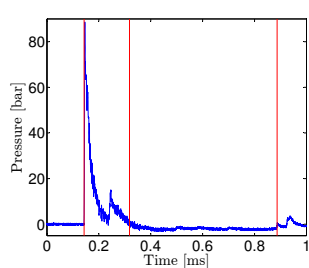
(a)



(b)

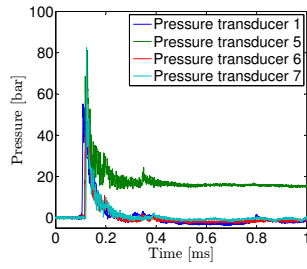


(c)

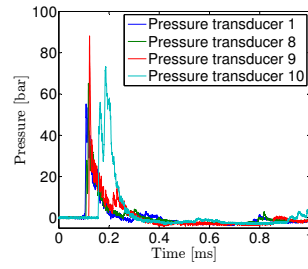


(d)

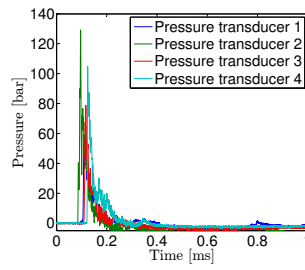
**Figure B.2:** Calibration R13 Pressure curves displaying second peak



(a)

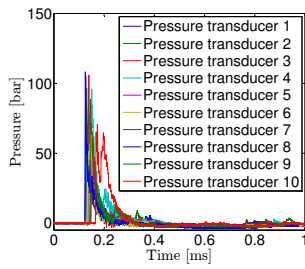


(b)

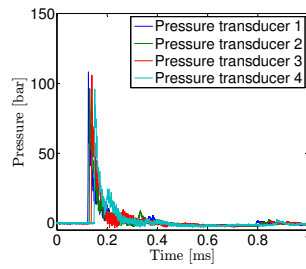


(c)

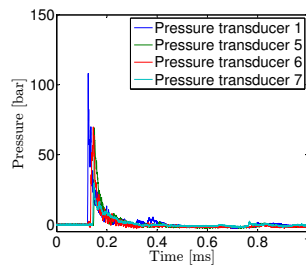
**Figure B.3:** Calibration R11 Time-pressure plots



(a)



(b)



(c)

**Figure B.4:** Calibration R13 Time-pressure plots

## **B.3    Calculated Impulses for Calibration Tests**



**Table B.1:** Postive and negative impulse and time of arrival for test R12

Sensor	Positive impulse [kPams]	Negative impulse [kPams]	$t_a$ [ms]
1	301	-31	0.1124
2	176	-143	0.1164
3	254	-67	0.1289
4	259	-92	0.1388
5	139	-90	0.1411
6	131	-82	0.1403
7	147	-43	0.1362
8	245	-103	0.1188
9	229	99.3	0.1383
10	-66	0.1710	

**Table B.2:** Postive and negative impulse and time of arrival for test R23

Sensor	Positive impulse [kPams]	Negative impulse [kPams]	$t_a$ [ms]
1	146	-148	0.2261
2	156	-68	0.2324
3	154	-68	0.2431
4	143	-20	0.2554
5	131	-18	0.2447
6	129	-15	0.2397
7	85	-36	0.2173
8	157	-8	0.2324
9	200	-60	0.224
10	230	-59	0.2677



# Appendix C

## Preliminary Study (Ch. 5)

## C.1 Keyword Example Abaqus/Explicit

```

*Heading

** Job name: Conwep_0125_usp Model name: Conwep_0125

** Generated by: Abaqus/CAE 6.12-2
#####

** PARTS

#####
*Part, name=PLATE

*Surface, type=ELEMENT, name=LOADING_AREA
_LOADING_AREA_SPOS_1, SPOS
** Section: Section-1-SET_PLATE

*Shell Section, elset=SET_PLATE, material=Docol600DL
0.0008, 5

*Transverse Shear
5.3846e+07, 5.3846e+07, 0.

*End Part
**
#####

** ASSEMBLY

#####
*Assembly, name=Assembly
**
*Instance, name=PLATE-1, part=PLATE
*End Instance
**

```

```

*Surface, type=ELEMENT, name=BLAST_SURFACE
_BLAST_SURFACE_SPOS_1, SPOS
*End Assembly

#####

** MATERIALS

#####

*Material, name=Docol600DL
*Density
7850.,
*Depvar, delete=46
    46,
*User Material, constants=22
1., 1., 0., 1., 0., 0., 0., 3.64e+06
0., 2.1e+11, 0.3, 3.27e+08, 7.837e+09, 0., 1.9345e+10, 7.893e+07
0., 0., 0., 0., 0., 0.

#####

** INTERACTION PROPERTIES

#####

*Incident Wave Interaction Property,
name=SHOCK_WAVE, type=AIR BLAST
*CONWEP Charge Property
0.0384, 1.
1., 1., 1.
**
#####

```

```

** BOUNDARY CONDITIONS

#####

** Name: Disp-BC-1 Type: Symmetry/Antisymmetry/Encastre
*Boundary
CLAMPED_EDGES, ENCASTRE
** Name: Disp-BC-2 Type: Symmetry/Antisymmetry/Encastre
*Boundary
EDGE-X_DIRECTION, XSYMM
** Name: Disp-BC-3 Type: Symmetry/Antisymmetry/Encastre
*Boundary
EDGE-Y_DIRECTION, YSYMM
** -----
**
** STEP: Blast
**
*Step, name=Blast
*Dynamic, Explicit
, 0.02
*Bulk Viscosity
0.06, 1.2
**
#####
*
** INTERACTIONS
**
#####

** Interaction: IncWave-1
*Incident Wave Interaction, CONWEP,
property=SHOCK_WAVE
BLAST_SURFACE, M_SET-4, , 0., 1.
**

```

#####

\*\* OUTPUT REQUESTS

#####

\*Restart, write, number interval=1, time marks=NO

\*\*

\*\* FIELD OUTPUT: F-Output-2

\*\*

\*Output, field, number interval=2000

\*Node Output

U,

\*Element Output, directions=YES

P, PEEQ

\*\*

\*\* FIELD OUTPUT: F-Output-1

\*\*

\*Element Output, elset=PLATE-1.SENSORS, directions=YES  
IWCONWEP, P

\*\*

\*\* HISTORY OUTPUT: H-Output-1

\*\*

\*Output, history

\*Energy Output

ETOTAL,

\*End Step



# Appendix D

## Keyword Example Impetus-Afea (Ch. 7)

## D.1 Keyword Example for Pre-Tensioning

D.2

```

*UNIT_SYSTEM
SI
*PARAMETER
A1   = 500.0e6
B1   = 500.0e6
n1   = 0.3
A3   = 800.0e6
B3   = 770.0e6
n3   = 0.5
s0   = 327.6e6      # Yield Stress
Q1   = 384e6        # Voce coefficient
C1   = 20.41        # Voce coefficient
Q2   = 78.93e6      # Voce coefficient
C2   = 245.1        # Voce coefficient
Wc   = 790.0e6
sig  = 534e6
term = 0.002
*INCLUDE
mesh.k
1.0e-3, 1.0e-3, 1.0e-3
*TIME
[%term], 0, 2.0e-7
*OUTPUT

0, 0, ALL
*CHANGE_P-ORDER
ALL, 0, 3
*MAT_METAL
1, 7800.0, 210.0e9, 0.3
1
*MAT_METAL
3, 7800.0, 210.0e9, 0.3
3
*MAT_METAL

```

```

8, 7800.0, 210.0e9, 0.3, 8
8
*FUNCTION
1
%A1 + %B1*epsp^%n1
*FUNCTION
3
%A3 + %B3*epsp^%n3
*FUNCTION
8
%s0 + %Q1*(1-exp(-%C1*epsp))+%Q2*(1-exp(-%C2*epsp))
*PROP_DAMAGE_CL
8, 2
[%Wc]
*SMOOTH_MESH
ALL, 0, 50.0
*PART
"mounting frame"
1, 1
"bolts"
3, 3
"diagonal beams"
4, 1
"clamping frame"
5, 1
"horizontal beams"
6, 1
"target plate"
8, 8
"connecting plates"
9, 1
*MERGE
"connectng plates -> frame"
P, 9, P, 1

```

```

"diagonal beams -> connecting plates"
P, 4, P, 9
"horizontal beams -> connecting plates"
P, 6, P, 9
"diagonal beams -> horizontal beams"
P, 4, P, 6
*BC_MOTION
"ground"
G, 100, XYZ
*GEOMETRY_BOX
100
0, -0.501, -2.0, 0, -0.499, -0.06
*CONTACT
"all -> all"
ALL, 0, ALL, 0, 0.3, 5.0e12
1
*LOAD_PRESSURE
GS, 1, 200
*BC_MOTION
G, 300, Z
*GEOMETRY_SEED_COORDINATE
300
0.3, 0, 0.003
*SET_GEOMETRY
1
1, 2, 3, 4, 5, 6, 7, 8
9, 10, 11, 12, 13, 14, 15, 16
*CURVE
200
0.0, 0.0
[%term/2], [-%sig]
[%term], [-%sig]
*GEOMETRY_SEED_COORDINATE
1

```

-0.125142, -0.175211, 0.00975494  
\*GEOMETRY\_SEED\_COORDINATE  
2  
-0.0625767, -0.175257, 0.0106331  
\*GEOMETRY\_SEED\_COORDINATE  
3  
-0.175253, -0.125155, 0.00966197  
\*GEOMETRY\_SEED\_COORDINATE  
4  
-0.175328, -0.0626032, 0.0106298  
\*GEOMETRY\_SEED\_COORDINATE  
5  
0.125136, -0.17523, 0.00984048  
\*GEOMETRY\_SEED\_COORDINATE  
6  
0.0625766, -0.175259, 0.01063  
\*GEOMETRY\_SEED\_COORDINATE  
7  
0.175268, -0.125161, 0.0098455  
\*GEOMETRY\_SEED\_COORDINATE  
8  
0.175348, -0.0626101, 0.0108229  
\*GEOMETRY\_SEED\_COORDINATE  
9  
-0.125163, 0.17528, 0.00978824  
\*GEOMETRY\_SEED\_COORDINATE  
10  
-0.0626008, 0.175366, 0.0108155  
\*GEOMETRY\_SEED\_COORDINATE  
11  
-0.175284, 0.125163, 0.0098504  
\*GEOMETRY\_SEED\_COORDINATE  
12  
-0.175348, 0.0625805, 0.0108342

```
*GEOMETRY_SEED_COORDINATE
13
0.125166, 0.175299, 0.0099841
*GEOMETRY_SEED_COORDINATE
14
0.062587, 0.175374, 0.0109214
*GEOMETRY_SEED_COORDINATE
15
0.175294, 0.125169, 0.0100307
*GEOMETRY_SEED_COORDINATE
16
0.175369, 0.0625815, 0.0109963
*LOAD_DAMPING
ALL, 0, 1000
*FUNCTION
1000
1000.0
*END
```

## D.2 Keyword Example for Blast Simulations



```

*UNIT_SYSTEM
SI
*PARAMETER
A1   = 500.0e6      # frame yield stress
B1   = 500.0e6      # frame hardening parameter
n1   = 0.3          # frame hardening parameter
A3   = 800.0e6      # bolt yield stress
B3   = 770.0e6      # bolt hardneing parameter
n3   = 0.5          # bolt hardening parameter
s0   = 327.6e6      # Yield Stress
Q1   = 384e6        # Voce coefficient
C1   = 20.41        # Voce coefficient
Q2   = 78.93e6      # Voce coefficient
C2   = 245.1        # Voce coefficient
Wc   = 790.0e6      # C-L failure parameter
soff = 0.125        # stand-off distance
R    = 0.01725      # charge radius
L    = 0.4          # air domain size parameter
term = 0.003        # termination time
*INCLUDE
../prestress/impetus_state1.k
*TIME
[%term]
*OUTPUT

0, 0, P, 8
*MAT_METAL
1, 7800.0, 210.0e9, 0.3
1
*MAT_METAL
3, 7800.0, 210.0e9, 0.3
3
*MAT_METAL
8, 7800.0, 210.0e9, 0.3, 8

```

```

8
*SMS_CLUSTER
P, 8, 10.0, 1.0e-3
*FUNCTION
1
%A1 + %B1*epsp^%n1
*FUNCTION
3
%A3 + %B3*epsp^%n3
*FUNCTION
8
%s0 + %Q1*(1-exp(-%C1*epsp))+%Q2*(1-exp(-%C2*epsp))
*PROP_DAMAGE_CL
8, 2
[%Wc]
*PART
"mounting frame"
1, 1
"bolts"
3, 3
"diagonal beams"
4, 1
"clamping frame"
5, 1
"horizontal beams"
6, 1
"target plate"
8, 8, 0, 0, 0, 1.0e-8
"connecting plates"
9, 1
*MERGE
"connectng plates -> mounting frame"
P, 9, P, 1
"diagonal beams -> connecting plates"

```

```

P, 4, P, 9
"horizontal beams -> connecting plates"
P, 6, P, 9
"diagonal beams -> horizontal beams"
P, 4, P, 6
"mounting frame -> bolts"
P, 1, P, 3, 1.0e-3
*BC_MOTION
"ground"
G, 100, XYZ
*GEOMETRY_BOX
100
0, -0.501, -2.0, 0, -0.499, -0.06
*CONTACT
"all -> all"
ALL, 0, ALL, 0, 0.3, 5.0e12
*PBLAST
ALL, 0, 1, 0, c4, 1000000
0, 0, 1, 0, 0, 0
2000, 0, 3000, 0.0, 0.0, [-0.0128-%soff], 0.0, 5.0e-4
*GEOMETRY_BOX
2000
[-%L], -0.5, [-0.0128-%soff-%L], [%L], [%L], 0.15
*GEOMETRY_SPHERE
3000
0, 0, [-0.0128-%soff], [%R]
*LOAD_DAMPING
ALL, 0, 1000
*CURE
1000
0.0, 0.0
1.0e-3, 0.0
1.1e-3, 1000.0
1.0, 1000.0

```

\*END